April 2021

Theory and Application of Dielectric Rod Antennas and Arrays

Gabriel Saffold
University of South Florida

Scholar Commons Citation

Saffold, Gabriel, "Theory and Application of Dielectric Rod Antennas and Arrays" (2021). *USF Tampa Graduate Theses and Dissertations.*
https://digitalcommons.usf.edu/etd/8857

Theory and Application of Dielectric Rod Antennas and Arrays

by

Gabriel Saffold

A dissertation submitted in partial fulfillment
of the requirements for the degree of
Doctor of Philosophy in Electrical Engineering
Department of Electrical Engineering
College of Engineering
University of South Florida

Co-Major Professor: Thomas Weller, Ph.D.
Co-Major Professor: Stephen Saddow, Ph.D.
Andrew Hoff, Ph.D.
Frank Pyrtle, III, Ph.D.
Abigail Bowers, Ph.D.

Date of Approval:
March 19, 2021

Keywords: Additive Manufacturing, Surface Wave Antennas, 3D Printing

Dedication

To my crazy wife, Shana, I have no idea how you handle all of everything. This dissertation is dedicated to you. It will help you fall asleep. This work has taken precious hours of attention and fun away from you and now you have to call me Doctor, or maybe Lord High Doctor. I don't make the rules. Sorry. Here's to even more adventures. I Love you. To Alex, Noah, JoJo, and Ella, I will put my laptop down now. Thanks for climbing all over me while I was writing and reading. Thank you for helping me work in the antenna chamber and for always reminding me to use 50 Ohms on absolutely everything electrical always. Thanks for demanding my attention and for paying me with hugs and kisses. No degree is worth even the smallest bit of missed time with you. I love you mostest.

Acknowledgment

I'd like to thank everyone who was very patient with me and who helped me navigate this process. First, to Dr. Weller for agreeing take me on as a student and for sticking with me from trying to remember basic engineering facts all the way through a doctoral defense. His patience is beyond explanation. To Dr. Saddow for agreeing to be my co-advisor and for being a constant source of knowledge and encouragement. To Dr. Bowers for her encouragement and guidance with the math involved in this work. To Dr. Pyrtle for rigorous and challenging conversations along the way. To Dr. Hoff for agreeing to join the committee and Dr. Wang to joining as the chair on short notice. To Dr. Collier from Oak Ridge for the PhD cartoons and guidance in Python and LaTeX. To Dr. Fountain and the USF Center for Entrepreneurship faculty and staff for their encouragement and guidance and for patiently keeping the academic machinations grounded in practical purpose. To the USF EE office staff for patiently fielding endless stupid questions, for always being up for some laughs, and for believing I would finish this PhD even when I didn't really believe it myself. To Dr. Braue and USF Veteran Services for having my back, helping me fill out simple, but rage-inducing forms, and for football games with my family. To USF for helping me to launch a military career and to recover from it: from unique and useful joint officer training to medical research that literally saved my life. To all of you and so many more, your help, kindness, and encouragement mattered more than I could ever express. Thanks.

Table of Contents

List of Tables

List of Figures

Abstract

Dielectric rods have been used for many years as waveguides and radiators. Their low loss as a transmission line and tendency to radiate at discontinuities have proven useful in applications ranging from fiber optic cables to naval fire control radar. Although this technology is well established, advances in additive manufacturing techniques and associated materials combined with the ubiquity of wireless communications and their shift to higher frequencies have generated renewed interest in dielectric rods. Dielectric rod antennas have moderate gain and less conductive loss at higher frequencies. Similar to other surface wave antennas, they can achieve broadband performance.

This work is the result of an effort to validate a concept for an array with greater than 20 dBi of gain for direct integration with a fully additive manufactured transmit/receive module at w-band. A literature review of high gain w-band antennas suited for this purpose reveals the dielectric rod antenna (DRA) as a suitable candidate. Further literature review examines the history and state of the art of DRAs as well as their underlying theory and accepted design procedures. The DRA field calculations here are generalized for a solid DRA surrounded by an infinite, generic medium. Rather than assume air in the outer medium, the calculations here keep the permittivity and permeability of the material outside the rod.

A planar-fed DRA is designed by analogy to the canonical design for high gain surface wave antennas presented in The Antenna Engineering Handbook [1]. Unlike all but one planar-integrated DRA in the literature, this planar-fed DRA does not use hollow metallic waveguide for electrical or mechanical support. The DRA is fed by a coplanar waveguide (CPW) fed folded-dipole slot antenna. The DRA has a $-10\ dB$ impedance bandwidth of 22%, radiation efficiency about 95%, 26° 3 dB beamwidth, and a gain of 16.5 dBi at 15 GHz. Even though the final application of these designs is intended to be at w-band, Ku-band DRAs are developed for ease of fabrication and measurement while also validating the underlying principles involved in their design.

A planar-fed, 2 x 2 square, four element DRA array with corporate feed is designed, simulated, fabricated, and measured using the single planar-fed design mentioned above. The fabricated array achieves a gain 19 *dBi* with a 3 *dB* gain bandwidth of 26%. The array is fabricated with 52 mm separation between elements with a radiation efficiency is 80%. The 4-element array is simple, cost-effective to fabricate, being made with standard PCB processes and 3D printed ABS plastic DRAs, and may be scaled into the mm-wave regime.

The final array gain of 19 dBi at 15 GHz is just 1 dB under the desired gain of 20 dBi. Future iterations of this design may take advantage of cladding in the dielectric rod antennas to further customize the size, footprint, weight, and robustness of the array by printing high dielectric constant rods embedded in lower dielectric, 3D printed cladding. The generic field equations are applied to DRA design in order to explore the design of cladded DRAs and the effect of cladding on DRA size and performance. The results suggest that the use of cladding in this DRA array design should bring the gain over the 20 dBi threshold while also making it possible to reduce the size of the array. The canonical maximum gain surface wave design procedure generally used for DRA design is modified to account for outer materials other than air or vacuum.

Chapter 1: Introduction

Communication systems, especially those related to 5G, are moving up into mm-wave bands where metal losses can become significant and many traditional fabrication and manufacturing techniques become more difficult. Dielectric rod antennas (DRA) are entirely made of dielectric and may be injection-molded or 3D-printed as solid rods, layered rods, or tubes. As communication technologies continue to move toward operation at higher frequencies, especially with the current push into mm-wave bands, dielectric rod antennas (DRA) are a good low-cost alternative for achieving high gain with minimal use of metal. Dielectric structures do not suffer from the losses associated with metallic structures of similar size. Dielectric rods, used in conjunction with an underlying radiating feed, increase the overall gain of the feed radiator and offer more flexibility in manufacturing. DRA arrays do not have as large of a footprint as planar antenna arrays with the same gain. However, they have a much larger profile, where profile is the direction normal to the surface of a planar circuit. This comparison is reviewed in Chapter 2 by comparing the volumes of DRA arrays to arrays with comparable gain.

A dielectric rod antenna array fed by slot antenna radiators without the use of metallic waveguide is presented here. Direct integration of dielectric rods onto planar circuit radiators is demonstrated with inexpensive, 3D printed ABS dielectric rods. Although these rods are not directly printed on the RF circuits in this work, the principle is validated. While the normal approach to feeding DRAs involves some version of metallic waveguide, we show here that the DRA may be integrated with a planar radiator feed and used effectively in an array configuration. The array demonstrated is a 2 x 2 array designed for operation at 15 GHz. Each DRA is 6λ long. The array is fabricated on a 100 mm x 100 mm substrate with 52 mm separation between elements. The array radiation efficiency is 80% for an array gain of 19 dBi, which is just 1 dBi below the stated gain objective. The use of cladding in DRA design is explored and validated as a solution for bringing the gain of the final array at or above the objective. Scale to w-band is left for future work. All simulations in this paper were performed using the Ansys High Frequency Structure Simulator (HFSS) version 2020R1.

DRAs have been used in radar antenna arrays [2, 3, 4], millimeter-wave imaging [5], and other applications [6, 7]. The feed mechanisms for the dielectric rods typically include some form of a metallic waveguide for support or for setting up the modes necessary for launching a surface wave along the rod. Most of these are hollow metallic waveguide-fed designs [5, 8, 9, 10, 11, 12, 13, 14, 15, 16, 17, 18]. In other designs, the metallic waveguide is used in conjunction with a planar radiator, as in [19, 20, 21, 22]. Chu and Kilcoyne [23] feed a DRA with a helix. Abumunshar and Sertel [24] as well as Liu and Chen [25] use a unique v-shaped two-wire TEM waveguide feed along a feed taper in the DRA. A DRA to DRA, on-chip communication system uses dielectric rod waveguide-fed DRAs [26]. Other planar-integrated DRAs have been fed without hollow metallic waveguides including those fed with an edge-fed design using antipodal Vivaldi antennas [6], a stacked patch [7], and direct contact between the DRA and a ring-slot [27]. Rivera-Lavado et al. [28, 29] demonstrate THz DRAs fed by integration of the dielectric rod with a planar, linearly polarized log-periodic radiator.

Several of the works referenced above include arrays: both with non-planar feeds [3, 5, 10, 15, 18] and planar-integrated feeds [19, 22]. While there are planar-fed DRAs without metallic waveguides, as mentioned above, there are no instances known to the authors of planar-integrated arrays of DRAs which do not use hollow metallic waveguides as part of the feed structure. This work fills that gap.

The metallic waveguide is advantageous for physical stability and for a more efficient launch of the surface wave along the rod. At lower frequencies, where metallic losses are insignificant and metal is easily formed, the use of a metallic waveguide with a planar feed may be preferable. However, the metallic waveguide is not necessary for a single element or an array of planar-fed DRAs.

Chapter 2 reviews the literature related to high gain, w-band arrays. This literature review reveals the DRA as an advantageous approach for their broadband response, moderate individual antenna gain performance, and compatibility with additive manufacturing techniques and additive manufactured circuits. The literature review then explores the state of the art of DRA and DRA array implementation and design. There are gaps in the literature related to feeding DRAs with structures that do not involve hollow metallic waveguides. This gap extends to the limited existing body of work of DRA arrays.

Chapter 3 mathematically evaluates the fields in dielectrics rods and develops the equations and relationships necessary for DRA design. In the literature, these equations assume the rod is surrounded by air or vacuum. Here, the outer material properties remain generic. The permeability and permittivity of the surrounding medium are maintained throughout. This enables the design of cladded DRAs. Further attention is given to the operating parameters and characteristics of the dielectric rod as an antenna.

Chapter 4 examines individual DRA design using a planar feed. The principles of maximum gain surface wave antenna design for a DRA fed with a hollow metallic waveguide are applied to a single DRA fed by a folded dipole slot antenna. The results suggest the need for modifications to the prediction of gain relative to the physical dimensions of the DRA. Otherwise, the design procedures and performance are similar between hollow metallic waveguide fed DRAs and planar fed DRAs. The planar-fed DRA has a gain of 16.5 *dBi* with a radiation efficiency of 96%.

An array of planar fed DRAs is presented in Chapter 5. The design principles for an array of maximum gain surface wave antennas is applied to the design, simulation, fabrication, and measurement of a unique 2 x 2, folded dipole slot-fed DRA array. As with the individual planar-fed DRA designs, the DRAs in the array do not use hollow metallic waveguides in the feed. The gain of the array is maximized by controlling the spacing between the individual elements. The array radiation efficiency is 80% at 15 GHz for an array gain of 19 dBi, which is only 1 dB lower than the 20 dBi gain objective. No modifications to the design method for a high gain surface wave antenna array were necessary.

Chapter 6 examines the the effect of changing the material immediately outside the DRA from air or vacuum to ABS. These DRAs are hollow metallic waveguide fed with rectangular cross-sections. The design procedures for maximum gain surface wave antennas are used to design each DRA making use of the generic field calculations of Chapter 3. The DRAs are made of high dielectric constant Rogers 3010, $\varepsilon_r = 10.2$. Comparisons are made between no cladding, $\varepsilon_r = 1$, 50% infil 3D printed ABS, $\varepsilon_r = 1.6$, and 100% infil 3D printed ABS, $\varepsilon_r = 2.6$. The DRAs are designed for the same gain, which results in a decrease in length for increased dielectric constant of the cladding. Also, as dielectric constant of the cladding increases, the cross-sectional area of the rod increases. The high gain surface wave antenna design procedures apply to the design of the cladded dielectric rods, although the prediction of the optimal length of the one of the DRA dimensions varies significantly from the length predicted by the existing design procedure. Further examination is necessary to determine if this phenomenon results from the addition of cladding or from the conversion between calculations of the dimensions of circular cross-section DRAs and the dimensions of rectangular cross-section rods. This is a subject for future work. The results of the work of Chapter 6 suggest that the addition of dielectric cladding to the planar-fed DRA array would bring the gain above the 20 dBi target value and may also allow some reduction of the array volume.

Chapter 7 summarizes opportunities for future work based on the outcomes detailed in this body of work. The accuracy of the conversion between circular cross-section DRA dimensions and rectangular cross-section DRA dimensions should be examined. The final DRA array design at w-band should be explored, as well as the addition of cladding to the DRA for increased gain. Ultimately, there is a place for the design and fabrication of a fully 3D printed transmit and receive module integrated with a planar-fed DRA array.

This work has resulted in several unique contributions. First, the application and evaluation of existing maximum gain surface wave antenna design procedures to planar-fed DRAs without hollow metallic waveguides resulted in a modified design procedure with more accurate prediction of planar-fed DRA gain. Second, A unique DRA array using the planar-fed DRA above was designed, simulated, fabricated, and measured. The performance of the array demonstrated good performance relative to the expected theoretical performance. Third, existing surface wave antenna design methods were applied to designing a DRA in cladding, or material other than air or vacuum. Modifications to the existing design procedure based on the field calculations of Chapter 3 resulted in a unique design procedure for cladded DRAs. The cladded DRA design procedure was validated through design, simulation, fabrication, and measurement of three different cladded DRAs as discussed above.

Chapter 2: Literature Review

As bandwidth and speed requirements increase in mobile communications, millimeter-wave bands have become more attractive. The FCC recently made large amounts of bandwidth available for millimeter wave communications, including those necessary for 5G operation [30]. High gain antennas are preferable at these frequencies to compensate for propagation loss over relevant distances while in some applications also conforming to small device sizes. The underlying objective of this work is to develop a radiator solution for integration with an additive manufactured transmit/receive module for point-to-point communications at w-band with a gain at or above 20 dBi. The following literature review examines available radiator options with gain above 20 dBi. DRAs are chosen as the solution for their compatibility with additive manufacturing techniques as well as moderate individual gain and the possibility for higher gain in an array configuration. The second half of the literature review examines the state of the art in DRA design toward understand gaps in the literature leading the unique contributions herein.

In order to compare w-band solutions, this review defines radiator and array size in relation to the plane of the surface of the system with which the antenna will be integrated. The size of the antenna in the plane of this surface is called the footprint. The size of the antenna perpendicular to the plane of the same surface is called the profile. A microstrip patch antenna (MSA) is low profile with variable footprint: it is small in the direction perpendicular to the surface of the system with which it is integrated, but may be large in the plane of the same surface as a single element or as an array. The microstrip patch antenna generally radiates in the direction of its profile. A linear tapered slot antenna radiates end-fire and is an example of a low profile, large footprint antenna with radiation primarily in the plane of its footprint, rather than in the direction of its profile. Physical dimensions and electrical performance are noted when reported by the authors.

2.1 Moderate to High Gain W-band Antennas

2.1.1 Microstrip Patch Antennas

A broadband and high gain tapered slot antenna for w-band imaging array applications [31]. The authors designed and simulated a tapered slot antenna with corrugated radiators matched to microstrip feed line with microstrip to co-planar stripline baluns. The antenna performance was demonstrated in the full w-band, 75 – 100 GHz, with low insertion loss and consistent gain of 14 dBi and HPBW of 30 degrees.

Cheng et al [32] designed and demonstrated a 32x32 element square patch antenna array fed by a substrate integrated waveguide network. The simulated gain of the array is reported to be 28.81-29.97 dBi between 91 and 97 GHz with a measured maximum gain of 29.97 dBi at 94 GHz. The footprint of the entire fabricated array structure is 92 x 66 mm2 while the surface area of the array is 63 x 63 mm2.

Ghassemi et al. [33] designed and fabricated a 4x4 patch antenna array fed by substrate integrated waveguide. An SIW T-junction and two Y-junctions are used to form a four-way power divider to feed the array. The SIW was implemented with both arrays. One array consisted of circular patch antennas fed by SIW with a dielectric rod layer above each row of four patches. The second antenna was similar but with Yagi-like parasitic director elements overlaying each of the four rows. The gain of both was 18 ± 1 dB. The measured impedance bandwidth of both arrays was 7.5 GHz. The radiation efficiency of the first design was 81% and the second 90%.

A millimeter-wave dual-polarized high-isolation antennas and arrays on organic substrates is presented [34] which includes an aperture-coupled patch antenna array. The design is dual polarized. Kapton and liquid crystal polymer are used to increase isolation between polarizations. The focus of this work was the utilization of organic materials in increasing isolation for a dual polarized antenna. Gain performance is expected to be similar to that of other microstrip patch antenna arrays.

The authors of ”A 94 GHz aperture-coupled micro-machined microstrip antenna” [35] present a cavity-backed aperture coupled microstrip square patch antenna at 94 GHz fed through the coupling slot by a coplanar waveguide. At 91 GHz, the antenna had an impedance bandwidth of 11%. Gain was not reported, but is expected to similar to other microstrip patch antenna arrays.

2.1.2 Aperture Antennas

in ”Etched-silicon micro-machined w-band waveguides and horn antennas” [36], the authors fabricated a diamond shaped waveguide by etching v-grooves in (100) silicon ending in a flared groove section in two halves and placing those halves together. When placed together, the two grooves created a diamond shaped waveguide ending in a horn antenna.

An 8x8 narrowband, 8.3% impedance bandwidth, slot antenna array achieved a gain of 26.8 dBi at 94 GHz [37]. The array is fed by a standing wave in a metal waveguide formed in an electroforming process. The footprint of the array is 473.1 mm^2 and the profile is less than 5 mm.

”Planar high-gain dielectric-loaded antipodal linearly tapered slot antenna for e-band and w-band gigabyte point-to-point wireless services” [38] details a mm-wave SIW-fed antipodal linear tapered slot antenna. The authors examine different profiles of dielectric loading. Rectangular loading produced a maximum gain for a single element of 14.5 dBi from 65 to 110 GHz with a rectangular dielectric length of 4mm. A 1 x 4 element array measured 19 dBi gain.

Gauthier et al. [39] publish an antenna using a hyperboloid sub-reflector and a main reflector of a series of reflectors with different focal lengths. The authors measured gain of up to 40 dBi in a profile smaller than a standard dual-reflector design. The radiation efficiency measured 33%.

A 90-100 GHz double folded slot antenna [40] is designed and fabricated with an integrated dielectric lens. The design achieved 20 Ohm impedance from 85-110 GHz.

A 32 x 32 array 94 GHz substrate integrated monopulse antenna array of slot radiators on SIW was designed and demonstrated, fed by a sum-difference comparator and a 16 way divider [41]. The array operated from 93-96 GHz with a peak gain of 25.8 dBi.

Arrebola and Toso [42] modelled a dual reflectarray antenna as a demonstration of a modular method for analyzing such antennas in the Ku and W-bands. Their analysis revealed similar performance between a parabolic reflector in these bands and a flat reflectarray. The antenna produced a half-power beamwidth of 3° and gain of 38.7 dBi at 94 GHz.

”An E-band partially corporate feed uniform slot array with laminated quasi double layer waveguide and virtual PMC terminations” [43] is a 16 x 16 element array of radiating slots of 4, 4 x 4 slot subarrays. The array has a measured gain of 32.4 dBi and antenna efficiency of 83% with $-3dB$ gain bandwidth of 9% at 83.5 GHz. The array has a footprint of 60 mm x 60 mm and a profile of 8.9 mm, not including the WR-12 waveguide feed.

An axially symmetric dual reflectarray antenna [44] is designed to replace hyperboloid or ellipsoid sub-reflectors by decreasing the size using photo-etching fabrication techniques. Gain is reported to be 32.6 dBi. The reflectarray has a 72 mm diameter footprint, not including the support structure, and 30.05 mm profile height.

2.1.3 Lens Antennas

A W-band high gain lens antenna is designed for metrology and radar applications [45]. The design is a circular horn antenna integrated with an ECCOSTOCK 0005 lens for increased gain. The antenna is fed by a WR-10 waveguide. A WR-10 to circular waveguide transition section transitions the feed into the circular waveguide antenna. Gain is reported to be above 30 dBi between 75 and 110 GHz, although the gain varies between 30 and 36 dBi over w-band.

Dudorov et al. [46] proposed and evaluate a design for a lens antenna fed by a WR-10 metallic waveguide. A metamaterial reduced-permittivity region with periodically etched holes was added to the radiating edge of the antenna to reduce parasitic reflections. $S_1 1$ measured greater than 15 dB across w-band. The reported directivity is 14 dB at 100 GHz.

2.1.4 Dielectric Rod Antennas

In ”Dielectric Rod Waveguide Antenna for W-band with Good Input Match,” [47] GaAs and fused sapphire dielectric rod waveguides with a matching taper inserted into a WR-10 waveguide and a single body taper along the remaining length of the rod for radiation were examined at w-band. Antenna radiation patterns were measured along with the frequency dependence of beamwidth and input match. The pattern was found to be similar to that of the open waveguide, the beamwidth and input match were less frequency dependent with the input match greater than 25 dB over the full w-band.

”High Permittivity Dielectric Rod Waveguide as an Antenna Array Element for Millimeter Waves” [18] is a study of the suitability of sapphire dielectric rod waveguide antennas for an array by reporting the coupling related to the spacing of the elements. A 2 x 2, 4 element array of hollow metallic waveguide fed sapphire DRAs is examined.

Generalov et al. [48] examined the use of a single dielectric rod waveguide antenna over the entire band from 75-1100 GHz by matching the antenna to different standard hollow metallic waveguides. The gain of the antenna is not reported. The antenna demonstrated an insertion loss less than -17 dB for the entire range using WR-10 (75-110 GHz), WR-8 (90-140 GHz), WR-5 (140-220 GHz), WR-3 (220-325 GHz), WR-2 (325-500 GHz), WR-1.5 (500-750 GHz), and WR-1 (750-1100 GHz). The WR-1.5 and WR-1 require a transition section to match the antenna to the waveguide. Each combination of DRA and hollow metallic waveguide feed used the same DRA, demonstrating the broadband nature of DRAs and their tendency of their input impedance to be limited by the underlying feed rather than by the inherent characteristics of the DRA itself.

Generalov et al. [49] designed a dielectric rod waveguide antenna for operation from 75-325 GHz. The gain is at least 10 dBi across the band. The insertion loss is better than 15 dB with a 10 dB beamwidth of 95° and 3 dB beamwidth of $50-60^\circ$.

2.1.5 Leaky Wave Antennas

A leaky wave antenna structure made of a dielectric block with periodic silver strips on top, recessed in a metal trough under a metallic horn structure was designed and demonstrated in the w-band [50]. The radiation at the strips forms a broadside array. The horn acts as an h-plane sectoral horn along the array of strips, narrowing the beamwidth and increasing the gain in the H-plane. The device is steerable by changing the frequency. At 81.5 GHz, the return loss measured 15 dB. The overall gain as a product of E-plane and H-plane gain measured 26 dB with sidelobe levels at least 25 dB below the main beam.

Table 2.1 summarizes the w-band solutions with moderate to high gain that are best fit for integration with planar circuits. The footprints of each are compared by the size of their electrical footprint. Their volume in terms of electrical dimensions are also expressed as a figure of merit for comparison. The profile dimensions for planar arrays are typically not reported. To facilitate the comparison, $1/4\lambda_0$ is added to the profile direction of each design such that the profile dimension for planar designs is $1/4\lambda_0$. For non-planar designs, $1/4\lambda_0$ is added to the actual size of their profile dimension. This may be considered a representation of the actual electrical standoff required by any antenna, though in this case it is primarily a mathematical convenience.

Table 2.1: Existing planar high gain w-band solutions

First Author	**Type**	**Number of Elements**	**Gain (dBi)**	**Radiation Efficiency(%)**	**Footprint (λ_0)**	**Volume (λ_0^3)**
Zhang [43]	Double layered slot antenna	256	32	84	12 x 13.4	40.2
Kim [37]	Slot array	64	27	82	7 x 7	12.25
Cheng [32]	Patch array	1024	30	23	29 x 21	152.25
Chapter 5	DRA array	4	19	80	5 x 5	156.25

2.2 Dielectric Rod Antennas

The dielectric rod antenna is best understood as a special case of a dielectric rod waveguide. As with all waveguides, the chief performance objective is to convey the energy in some mode from an input feed point to an output point with minimal loss. Kiely [51] credits work by Hondros and Debye [52] as the earliest theoretical treatment of the use of a solid dielectric cylinder to convey electromagnetic energy from one port to another with low loss.

Early experimental work with dielectric cylinders as waveguides revealed their tendency to radiate at bends and discontinuities. Kiely credits unpublished work by Mallach as referenced by Zinke as the first effort to exploit the tendency to radiate at discontinuities by exciting a dielectric cylinder at one end and examining the radiation from the discontinuity at the other end. This configuration resulted in a single lobed end-fire radiation pattern in the direction of the cylinder axis with a proportional relationship between the length of the rod and the directivity of the radiation pattern. Several theories have been proposed to explain the radiation characteristics from a dielectric rod, including the mechanism of radiation and its relationship with rod material characteristics and dimensions for both uniform and tapered rods.

The radiation characteristics of dielectric rod antennas have been explained using variations on Huygens' principle and ray tracing methods [53, 3], by analogy to a dielectric lens [54], by calculation of fictitious surface currents along the surface of the rod using the Schelkunoff Equivalence Principle [55, 51], leaky-wave theory [56, 57], and by the discontinuity radiation concept [58, 59, 60, 1]. The discontinuity radiation concept is used in Zucker's design method for DRAs [1]. The analysis here is based on Zucker's method.

Huygens' principle with ray tracing theory uses constant phase wave fronts represented by vectors either reflecting or refracting at the outer interface of the rod, at the step discontinuity between inner and outer dielectric constants [53, 3]. Reflected waves continue to travel along the rod while refracted waves radiate from the surface of the rod and contribute to the far-field pattern. Wilkes' degenerate dielectric lens approach is similar [54]. These theories match well with experimental results in the main beam, but do not match well outside the first null beamwidth [51].

Watson and Horton use the Schelkunoff Equivalence Principle to explain dielectric rod radiation from a metallic waveguide-fed, rectangular cross-section dielectric rod. One iteration [55] begins with the assumption that radiation from a dielectric rod results from a standing wave along the rod. A second iteration [61] of their analysis assumes a travelling wave along the rod. An exact representation of the fields and currents on the surface of a rectangular cross-section rod is difficult. Horton [62] also examined uniform rods of circular cross-section. In each case, they calculate radiation patterns on the basis of electromagnetic fields produced from fictitious electric and magnetic surface currents along uniform dielectric rods. In the first two cases, they determine the results have good agreement with experiment for uniform rods between 3λ and 6λ long and significant disagreement with experiment beyond 6λ. Horton's application of this theory to a cylindrical rod [62], as with the other two cases, ignores radiation from the ends of the rod. Unlike the other two cases, the case of the cylindrical rod does not agree well with experiment without a correction factor applied to reduce the diameter used in calculation from the actual diameter of the rod. This adjustment dramatically improves agreement.

Since characterizations of dielectric rod waveguides have shown them to have very low loss along the length of the rod [63, 64], James [59] modified Horton's cylindrical rod calculations by including the ends of the rod in the calculations and assuming no radiation along the length of the rod. This rearrangement agrees well with Horton's published empirical data, without the need for the adjustment factor applied to the diameter of the rod. In general, for uniform cross-section rods, methods which negate or minimize the contribution of radiation from the feed and termination ends of the rod are the least accurate when compared to experimental results.

Brown and Spector [58] proposed a theory based on the idea that radiation does not occur along the length of a uniform rod, leaving radiation to occur only at discontinuities. For a uniform rod, the discontinuities are at the feed and terminal points. At the terminal point, the surface wave fields, which necessarily extend outward beyond the surface of the rod, form an aperture much like the aperture at the opening of a metallic horn antenna. This terminal aperture is larger than the cross-sectional area of the rod and can be used to calculate the fields of the radiation pattern. However, accounting for radiation only from the end of the rod does not produce good agreement with radiation measurements, nor does it account for the major discontinuity at the rod feed. When the total fields at the terminal aperture include both those resulting from the surface wave and also those resulting from the radiation at the feed, the agreement between theory and experiment improves. In particular, the addition of contributions to the fields at the terminal aperture from the fields at the feed creates a better predictor of the location of the first nulls and, consequently, the DRA's beamwidth and gain. James [59] notes an error in Brown and Spector's calculations. Correcting the error results in better agreement between the calculation and experimental results. The method has been reviewed [60] and experimentally verified [65]. It is also the basis for modern surface wave antenna design [1].

The method applies also to rods with successive discontinuities. Rather than a continuous taper, Simon and Weill [66] use conducting disks of decreasing diameter, which act as successive discontinuities creating radiating fields that contribute to the fields at the terminal aperture, thereby affecting the overall radiation pattern. Radiation from smooth, continuous tapers, on the other hand, behave according to the leaky wave antenna theories discussed by Watson [55] as validated by Brown and Spector [58] and James [59], since continuous tapers are continuous discontinuities.

Brown and Spector [58] also established a link between half power beamwidth and relative phase velocity as expressed in terms of the ratio of wavelengths outside and inside the rod, which is also the ratio between the inner and outer wave velocities. This is an important relationship, along with the link between cross-sectional dimension and relative phase velocity, which forms the foundation of DRA design and the ability to dictate DRA performance through careful design of the rod's physical dimensions.

Studies of attenuation along dielectric rods led to expressions of the relative phase velocities between a wave outside and inside the rod as a function of cross-sectional rod dimensions [63, 64, 51]. Similar studies carried out by Astrahan [67] and Jakes [68] explored attenuation along a dielectric tube and found a connection between the two, revealing the dielectric rod as a special case of a dielectric tube, wherein a rod is a tube in which the radius of the innermost, lower dielectric constant cylinder is reduced to zero leaving the higher dielectric outer shell of the tube as the material of the solid rod. The results for attenuation along the rod yield expressions for the relationship between phase velocities along the rod and the cross-sectional dimensions of the rod. These relationships facilitate control over the phase velocity through specification of cross-sectional dimensions, as in Figure 2.1 for different values of DRA permittivity ε_r. The curves in Fig. 2.1 are calculated using numerical methods to solve for the attenuation along the rod as in [64].

The majority of published dielectric rod antennas are fed by metallic waveguides. Planar feeds have been demonstrated, but not explored in detail. Furthermore, there is no example known to the authors of a planar-fed DRA array. The background and theory laid out above are necessary to understanding the role the feed plays in the function and design of a single DRA and of the consequences of this design to that of an array. This understanding results in design procedures for planar-fed DRA arrays. With this foundation in place, future DRA arrays may be designed including the possibility for fully additive manufactured, moderate to high gain arrays.

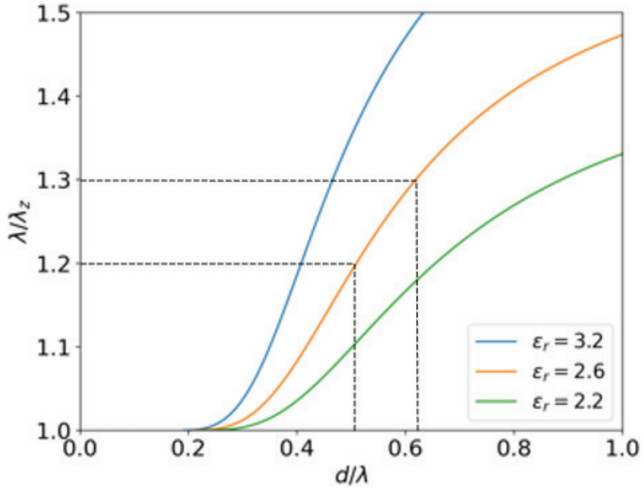

Figure 2.1: Design curves for cylindrical DRAs at 15 GHz. These relate the relative wavelength, $\frac{\lambda}{\lambda_z}$, to the cross-sectional diameter. Curves for three different rod dielectric constants are shown: $\varepsilon_r = 3.2$, $\varepsilon_r = 2.6$, and $\varepsilon_r = 2.2$. The DRA used in this work has $\varepsilon_r = 2.6$. The lower and upper limits of the recommended value for $\frac{\lambda}{\lambda_z}$ at the feed of a surface wave antenna are marked.

Table 2.2: Planar-integrated DRA arrays without waveguide

First Author	**Type**	**Number of Elements**	**Reported Gain (dBi)**	**Theoretical Gain (dBi)**	**Length (λ_0)**
Hanham [27]	Ring slot fed	1	12	13	2
Ahmad [20]	Slot with waveguide	1	11	12	1.4
Huang [69]	Patch with waveguide	1	16	18	6
Poprawa [21]	Microstrip coupled slot w/waveguide	1	18	21	13
Chapter 4	Slot-fed DRA	1	16	18	6
Liu [70]	Patch w/ waveguide DRA Array	16	20	25	2
Chapter 5	Slot-fed DRA array	4	19	22	6

Chapter 3: Dielectric Rod Antenna Design

3.1 Fields in Dielectric Rods

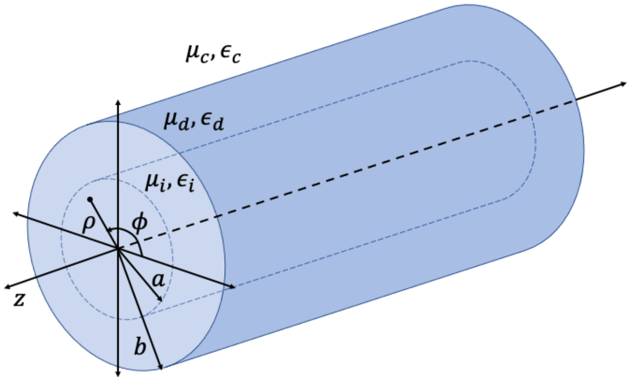

Figure 3.1: Generic dielectric rod. This rod is representative of both the dielectric rod and the cladded dielectric rod. The subscripts *d* and *c* refer to the dielectric and cladding sections of the generic dielectric rod.

The dielectric rod antenna (DRA) is a special case of a dielectric rod waveguide. The dielectric rod waveguide is a low-loss waveguide made of one or more layers of dielectric material. In the absence of discontinuities along the rod, such as bends, steps, and tapers, the dielectric rod waveguide does not radiate. The goal of dielectric rod antenna design is to intentionally create discontinuities to produce desirable radiation characteristics from the rod. Figure 3.1 illustrates a generic dielectric rod waveguide. This waveguide has three layers: an inner core (μ_i,ε_i), an outer dielectric (μ_d,ε_d), and an outer cladding (μ_c,ε_c).

Figure 3.1 represents three forms of dielectric rods. In the case $\varepsilon_d > \varepsilon_c \geq \varepsilon_i$ and $b > a > 0$, the dielectric rod is a dielectric tube [67, 68, 51]. Where $\varepsilon_d > \varepsilon_c = \varepsilon_0$ and $a = 0$, the structure is a dielectric rod. In the case of $\varepsilon_d > \varepsilon_c > \varepsilon_0$ and $a = 0$, the dielectric rod is a cladded dielectric rod, as discussed in Chapter 6. Dielectric tube antennas were briefly explored as a possible solution for planar-fed DRAs, but they are not discussed here.

DRAs are the primary focus of this work: planar-fed DRAs, planar-fed DRA arrays, and cladded DRAs. The equations necessary for designing DRAs are derived by analysis of waves within a cylindrical dielectric rod. The analysis begins with the the mathematical representation of the relationship between electric and magnetic fields found in Maxwell's equations. The following equations are the general form of Maxwell's equations.

$$\nabla \times \mathbf{E} = -\mathbf{M}_i - \frac{\partial \mathbf{B}}{\partial t} \tag{3.1}$$

$$\nabla \times \mathbf{H} = \mathbf{J}_i + \mathbf{J}_c + \frac{\partial \mathbf{D}}{\partial t} \tag{3.2}$$

$$\nabla \cdot \mathbf{D} = q_{ev} \tag{3.3}$$

$$\nabla \cdot \mathbf{B} = q_{mv} \tag{3.4}$$

where [71]

$\mathbf{E}$ = electric field intensity (volts/meter)

$\mathbf{H}$ = magnetic field intensity (amperes/meter)

$\mathbf{D}$ = electric flux density (coulombs/square meter)

$\mathbf{B}$ = magnetic flux density (webers/square meter)

$\mathbf{J}_i$ = impressed electric current density (amperes/square meter)

$\mathbf{J}_c$ = conduction electric current density (amperes/square meter)

$\mathbf{M}_i$ = impressed magnetic current density (volts/square meter)

q_{ev} = electric charge density (coulombs/cubic meter)

q_{mv} = magnetic charge density (webers/cubic meter)

$$\nabla^2 \mathbf{E} = -\omega^2 \mu \varepsilon \mathbf{E} \tag{3.5}$$

$$\nabla^2 \mathbf{H} = -\omega^2 \mu \varepsilon \mathbf{H} \tag{3.6}$$

The electric and magnetic Fields in a homogeneous region with constant μ and ε are defined by (3.5) and (3.6) where the time dependence, $e^{j\omega t}$ is assumed throughout. Solutions to each z component of the E and H fields in the form of (3.6) in each region are

$$E_{zm} = A_m J_m(k_m\rho) + B_m J_m'(k_m\rho)e^{-j\beta z} \tag{3.7}$$

$$H_{zm} = C_m J_m(k_m\rho) + D_m J_m'(k_m\rho)e^{-j\beta z} \tag{3.8}$$

Evaluating these equations for a conducting cylindrical tube with perfectly conducting boundary walls in cylindrical coordinates in a source and charge-free region leads to equations which describe the fields travelling inside the conducting tube [71]. Selecting only the terms in these equations which have simultaneous $cos(m/phi)$ variation in the E_z field component and $sin(m\phi)$ variation in the H_z component result in expressions for the fields in a dielectric rod, where $a = 0$ in Fig. 3.1.

For HEM modes in the rod material ($\rho \leq b$):

$$E_\rho^d = -j\frac{1}{\left(\beta_\rho^d\right)^2}\left[m\omega\mu_d A_m \frac{1}{\rho} J_m(\beta_\rho^d\rho) + \beta_z\beta_\rho^d B_m J_m'(\beta_\rho^d\rho)\right] cos(m\phi)e^{-j\beta_z z} \tag{3.9}$$

$$E_\phi^d = j\frac{1}{\left(\beta_\rho^d\right)^2}\left[\omega\mu_d\beta_\rho^d A_m \frac{1}{\rho} J_m'(\beta_\rho^d\rho) + m\beta_z B_m \frac{1}{\rho} J_m(\beta_\rho^d\rho)\right] sin(m\phi)e^{-j\beta_z z} \tag{3.10}$$

$$E_z^d = B_m J_m(\beta_\rho^d\rho)cos(m\phi)e^{-j\beta_z z} \tag{3.11}$$

$$H_\rho^d = -j\frac{1}{\left(\beta_\rho^d\right)^2}\left[\beta_z\beta_{rho}^d A_m J_m'(\beta_\rho^d\rho) + m\omega\varepsilon_d B_m \frac{1}{\rho} J_m(\beta_\rho^d)\right] sin(m\phi)e^{-j\beta_z z} \tag{3.12}$$

$$H_\phi^d = -j\frac{1}{\left(\beta_\rho^d\right)^2}\left[m\beta_z A_m \frac{1}{\rho} J_m(\beta_\rho^d\rho) + \omega\varepsilon_d\beta_\rho^d B_m J_m(\beta_\rho^d\rho)\right] cos(m\phi)e^{-j\beta_z z} \tag{3.13}$$

$$H_z^d = A_m J_m(\beta_\rho^d\rho)sin(m\phi)e^{-j\beta_z z} \tag{3.14}$$

$$(\beta_\rho^d)^2 + \beta_z^2 = \beta_d^2 = \omega^2\mu_d\varepsilon_d = \omega^2\mu_0\mu_{rd}\varepsilon_0\varepsilon_{rd} \tag{3.15}$$

$$Am = -j\frac{(\beta_\rho^d)^2}{\omega\mu_d\varepsilon_d}A_{mn}D_2 \tag{3.16}$$

$$Bm = -j\frac{(\beta_\rho^d)^2}{\omega\mu_d\varepsilon_d}B_{mn}C_2 \tag{3.17}$$

$$' \equiv \frac{\partial}{\partial(\beta_\rho^d\rho)} \tag{3.18}$$

For HEM modes in the outer medium ($\rho \geq b$), with β_z along the rod higher than β_0 outside the rod, the fields decay in the radial (ρ) direction. Therefore, the functions chosen to represent the fields outside the rod are modified Bessel functions, K_m, of the second kind of order m as in [71]:

$$E_\rho^c = j\frac{1}{\left(\alpha_\rho^c\right)^2}\left[m\omega\mu_c C_m\frac{1}{\rho}K_m(\alpha_\rho^c\rho) + \beta_z\alpha_\rho^c D_m K_m'(\alpha_\rho^c\rho)\right]cos(m\phi)e^{-j\beta_z z} \tag{3.19}$$

$$E_\phi^c = -j\frac{1}{\left(\alpha_\rho^c\right)^2}\left[\omega\mu_c\alpha_\rho^c C_m K_m'(\alpha_\rho^c\rho) + m\beta_z D_m\frac{1}{\rho}K_m(\alpha_\rho^c\rho)\right]sin(m\phi)e^{-j\beta_z z} \tag{3.20}$$

$$E_z^c = D_m K_m(\alpha_\rho^c\rho)cos(m\phi)e^{-j\beta_z z} \tag{3.21}$$

$$H_\rho^c = j\frac{1}{\left(\alpha_\rho^c\right)^2}\left[\beta_z\alpha_{rho}^d C_m K_m'(\alpha_\rho^c\rho) + m\omega\varepsilon_c D_m\frac{1}{\rho}K_m(\alpha_\rho^c)\right]sin(m\phi)e^{-j\beta_z z} \tag{3.22}$$

$$H_\phi^c = j\frac{1}{\left(\alpha_\rho^c\right)^2}\left[m\beta_z C_m\frac{1}{\rho}K_m(\alpha_\rho^c\rho) + \omega\varepsilon_c\alpha_\rho^c D_m K_m(\alpha_\rho^c\rho)\right]cos(m\phi)e^{-j\beta_z z} \tag{3.23}$$

$$H_z^c = C_m K_m(\alpha_\rho^c\rho)sin(m\phi)e^{-j\beta_z z} \tag{3.24}$$

$$(j\alpha_\rho^c)^2 + \beta_z^2 = -(\alpha_\rho^c)^2 + \beta_z^2 = \beta_c^2 = \omega^2\mu_c\varepsilon_c = \omega^2\mu_c\mu_{rc}\varepsilon_c\varepsilon_{rc} \tag{3.25}$$

$$' \equiv \frac{\partial}{\partial(\alpha_\rho^c\rho)} \tag{3.26}$$

For the dielectric rod in the absence of the perfectly conducting boundary conditions of the hollow metal tube, the following boundary conditions apply:

$$E_\phi^d(\rho = b, 0 \leq \phi \leq 2\pi, z) = E_\phi^c(\rho = b, 0 \leq \phi \leq 2\pi, z) \tag{3.27}$$

$$E_z^d(\rho = b, 0 \leq \phi \leq 2\pi, z) = E_z^c(\rho = b, 0 \leq \phi \leq 2\pi, z) \tag{3.28}$$

$$H_\phi^d(\rho = b, 0 \leq \phi \leq 2\pi, z) = H_\phi^c(\rho = b, 0 \leq \phi \leq 2\pi, z) \tag{3.29}$$

$$H_z^d(\rho = b, 0 \leq \phi \leq 2\pi, z) = H_z^c(\rho = b, 0 \leq \phi \leq 2\pi, z) \tag{3.30}$$

The result of applying these boundary conditions are as follows:

$$\begin{aligned}
&\frac{1}{(\beta_\rho^d)^2}\left[\omega\mu_d\beta_\rho^d A_m J'_m(\beta_\rho^d b) + m\beta_z B_m \frac{1}{b} J_m(\beta_\rho^d b)\right] = \\
&-\frac{1}{(\alpha_\rho^c)^2}\left[\omega\mu_c\alpha_\rho^c C_m K'_m(\alpha_\rho^c b) + m\beta_z D_m \frac{1}{b} K_m(\alpha_\rho^c b)\right]
\end{aligned} \tag{3.31}$$

$$B_m J_m(\beta_\rho^d b) = D_m K_m(\alpha_\rho^c b) \tag{3.32}$$

$$\begin{aligned}
&-\frac{1}{(\beta_\rho^d)^2}\left[m\beta_z A_m \frac{1}{b} J_m(\beta_\rho^d b) + \omega\varepsilon_d\beta_\rho^d B_m J'_m(\beta_\rho^d b)\right] = \\
&\frac{1}{(\alpha_\rho^c)^2}\left[m\beta_z C_m \frac{1}{b} K_m(\alpha_\rho^c b) + \omega\varepsilon_c\alpha_\rho^c D_m K'_m(\alpha_\rho^c b)\right]
\end{aligned} \tag{3.33}$$

$$A_m J_m(\beta_\rho^d b) = C_m K_m(\alpha_\rho^c b) \tag{3.34}$$

The following arrangements, following those made Balanis [71], are made in order to facilitate solving the preceding system of equations. At this point, existing literature makes the assumption that the outer material is air or vacuum. This is practically true for most DRA implementations. For the sake of evaluating the dielectric rod cladded in air, $\mu_c = \mu_0$ and $\varepsilon_c = \varepsilon_0$. However, in order to facilitate the evaluation of DRA design in outer materials other than air, the generic permeability and permittivity of the outer material are retained throughout the mathematical analysis here. According to (3.15) and (3.25):

$$(\beta_\rho^d)^2 + \beta_z^2 = \beta_d^2 \implies (\beta_\rho^d b)^2 + (\beta_z b)^2 = (\beta_d b)^2 \implies \beta_z b = \sqrt{(\beta_d b)^2 - (\beta_\rho^d b)^2} \tag{3.35}$$

$$-(\alpha_\rho^c)^2 + \beta_z^2 = \beta_c^2 \implies -(\alpha_\rho^c b)^2 + (\beta_z b)^2 = (\beta_c b)^2 \tag{3.36}$$

$$\chi = \beta_\rho^d b \tag{3.37}$$

$$\xi = \alpha_\rho^c b \tag{3.38}$$

$$\zeta = \beta_z b \tag{3.39}$$

$$\beta_d = \beta_0 \sqrt{\varepsilon_{rd}\mu_{rd}} \tag{3.40}$$

Subtracting (3.36) from (3.35) results in

$$\begin{aligned}(\beta_\rho^d b)^2 + (\alpha_\rho^c b)^2 = (\beta_d b)^2 - (\beta_c b)^2 \implies \alpha_\rho^c b &= \sqrt{(\beta_d b)^2 - (\beta_c b)^2 - (\beta_\rho^d b)^2} \\ &= \sqrt{(\beta_0 b)^2(\varepsilon_{rd}\mu_{rd} - \varepsilon_{rc}\mu_{rc}) - (\beta_\rho^d b)^2}\end{aligned} \tag{3.41}$$

Using (3.35) and (3.41):

$$\zeta = \sqrt{(\beta_0 b)^2 \varepsilon_r \mu_r - \chi^2} \tag{3.42}$$

$$\xi = \sqrt{(\beta_0 b)^2(\varepsilon_{rd}\mu_{rd} - \varepsilon_{rc}\mu_{rc}) - \chi^2} \tag{3.43}$$

To find solutions using these abbreviations, the system of equations (3.31) through (3.34) are written in the matrix form:

$$Fg = 0 \tag{3.44}$$

where:

$$F = \begin{bmatrix} \frac{\omega\mu_d b}{\chi} J'_m(\chi) & \frac{m\zeta}{\chi^2} J_m(\chi) & \frac{\omega\mu_0 b}{\xi} K'_m(\xi) & \frac{m\zeta}{\xi^2} K_m(\xi) \\ 0 & J_m(\chi) & 0 & -K_m(\xi) \\ \frac{m\zeta}{\chi^2} J_m(\chi) & \frac{\omega\varepsilon_d b}{\chi} J'_m(\chi) & \frac{m\zeta}{\xi^2} K_m(\xi) & \frac{\omega\varepsilon_0 b}{\xi} K'_m(\xi) \\ J_m(\chi) & 0 & -K_m(\xi) & 0 \end{bmatrix} \tag{3.45}$$

$$g = \begin{bmatrix} A_m \\ B_m \\ C_m \\ D_m \end{bmatrix} \tag{3.46}$$

Eq. (3.44) is satisfied where the determinate of F = 0 resulting in

$$\begin{aligned} F = & \frac{\omega^2 \mu_d \varepsilon_d b^2}{\chi^2} [J_m'(\chi)]^2 [K_m(\xi)]^2 + \frac{\omega \mu_d \varepsilon_c b^2}{\chi \xi} J_m(\chi) J_m'(\chi) K_m(\xi) K_m'(\xi) \\ & - \frac{(m\zeta)^2}{\chi^4} [J_m(\chi)]^2 [K_m(\xi)]^2 - \frac{(m\zeta)^2}{\chi^2 \xi^2} [J_m(\chi)]^2 [K_m(\xi)]^2 \\ & + \frac{\omega^2 \mu_c \varepsilon_d b^2}{\chi \xi} J_m(\chi) J_m'(\chi) K_m(\xi) K_m'(\xi) + \frac{\omega^2 \mu_c \varepsilon_c b^2}{\xi^2} [J_m(\chi)]^2 [K_m'(\xi)]^2 \\ & - \frac{(m\zeta)^2}{\chi^2 \xi^2} [J_m(\chi)]^2 [K_m(\xi)]^2 - \frac{(m\zeta)^2}{\xi^4} [J_m(\chi)]^2 [K_m(\xi)]^2 = 0 \end{aligned} \tag{3.47}$$

Dividing (3.47) by $\omega^2 \mu_0 \varepsilon_d a^2 [K_m(\xi)]^2$ allows the determinate to be arranged in the following form:

$$G_1(\chi) G_2(\chi) - G_3^2(\chi) = 0 \tag{3.48}$$

where

$$G_1(\chi) = \frac{\sqrt{\mu_{rd}} J_m'(\chi)}{\chi} + \frac{\sqrt{\mu_{rd}} \varepsilon_c K_m'(\xi) J_m(\chi)}{\varepsilon_d \xi K_m(\xi)} \tag{3.49}$$

$$G_2(\chi) = \frac{\sqrt{\mu_{rd}} J_m'(\chi)}{\chi} + \frac{\mu_{rc} K_m'(\xi) J_m(\chi)}{\sqrt{\mu_{rd}} \xi K_m(\xi)} \tag{3.50}$$

$$G_3(\chi) = \frac{m\zeta}{\beta_0 b \sqrt{\varepsilon_{rd}}} J_m(\chi) \left(\frac{1}{\chi^2} + \frac{1}{\xi^2} \right) \tag{3.51}$$

$$\zeta = \sqrt{(\beta_0 b)^2 \varepsilon_{rd} \mu_{rd} - \chi^2} \tag{3.52}$$

$$\xi = \sqrt{(\beta_0 b)^2 (\varepsilon_{rd} \mu_{rd} - \varepsilon_{rc} \mu_{rc}) - \chi^2} \tag{3.53}$$

As long as the eigenvalues, χ of (3.48), remain small enough for (3.53) to remain real, the fields outside the rod decay exponentially in the transverse direction. This is a necessary condition for surface wave propagation along the rod. Therefore, for every value of m, a finite number of solutions, χ_{mn}, exist which result in a surface wave along the dielectric rod. The value of eigenvalue for the HEM_{11} (HE_{11}) mode is $\chi_{10} = 0$. Therefore, the HE_{11} mode is the dominate mode. The next eigenvalue, χ_{01}, corresponds to the next modes to propagate along the rod. These are the TE_{01}, TM_{10}, and $HEM_{21}(HE_{21})$. According to (3.53), $\chi^2+\xi^2$ must be constant. In order to maintain the dominate mode, the constant of (3.54) should be less than the second eigenvalue squared.

$$\chi^2+\xi^2 = (\beta_0 b)^2(\varepsilon_{rd}\mu_{rd} - \varepsilon_{rc}\mu_{rc}) = constant < (\chi_{01})^2 \tag{3.54}$$

Eq. (3.54) can be rearranged to give the maximum diameter of a cylindrical dielectric rod above which modes higher than the dominant mode begin to propagate:

$$\frac{2b}{\lambda_0} < \frac{\chi_{01}}{\pi\sqrt{\varepsilon_{rd}\mu_{rd} - \varepsilon_{rc}\mu_{rc}}} \tag{3.55}$$

For a dielectric rod surrounded by air, $\chi_{01} = 2.4049$. Eq. (3.55) in it's generic form is useful for determining values of the diameter of the rod, based on values of χ and ξ as in (3.56). Further rearrangement gives an expression of $\frac{\lambda_0}{\lambda_z}$ for the same value of χ and ξ for a particular mode, frequency, and rod dielectric constant. Since $\frac{\lambda_0}{\lambda_z}$ is equivalent to $\frac{c}{v}$, the relationship between the phase velocity outside the rod and along the rod may be controlled by choosing values for the rod diameter, $2b$.

$$\frac{2b}{\lambda_c} = \frac{1}{\pi}\sqrt{\frac{\chi^2+\xi^2}{\varepsilon\mu - 1}} \tag{3.56}$$

$$\frac{\lambda_c}{\lambda_z} = \sqrt{\frac{\chi^2+\xi^2\cdot\varepsilon\mu}{\chi^2+\xi^2}} \tag{3.57}$$

$$\lambda_c = \frac{\lambda_0}{\sqrt{\mu_{rc}\varepsilon_{rc}}} \tag{3.58}$$

$$\varepsilon = \frac{\varepsilon_{rd}}{\varepsilon_{rc}};\ \mu = \frac{\mu_{rd}}{\mu_{rc}} \tag{3.59}$$

These final equations are necessary for DRA design. They allow the designer to control the electrical and radiation characteristics of the DRA through rigorous determination of the physical dimensions of the rod. In particular, diameter variations determine the modes of operation of the rod.

3.2 Dielectric Rods as Antennas

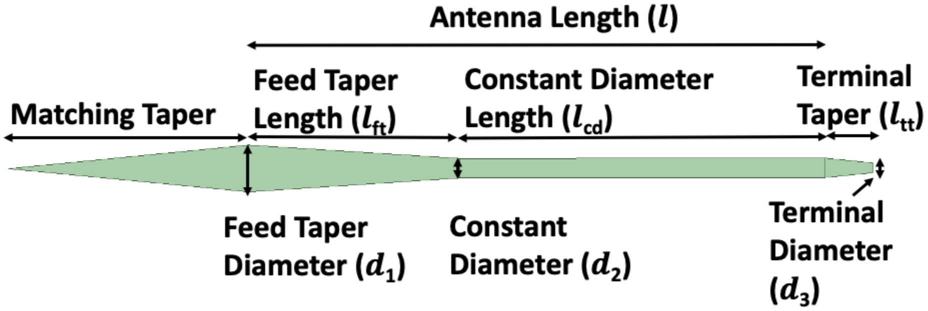

Figure 3.2: Maximum gain design for DRA as a surface wave antenna.

As an antenna, the DRA is designed by analogy to other surface wave antennas. In particular, much of the standard method for designing DRAs has been developed on the basis of theoretical and experimental work on long Yagi-Uda antennas [1]. The design methods are discussed in more detail in the following chapters in the development of planar-fed, planar-fed array, and cladded DRA design methods. This section constitutes a summary of the relevant antenna parameters of DRAs and existing, standard surface wave antenna design methodology that is typically applied to DRA design.

Surface wave antennas, including DRAs, may have constant cross-sections along their length or may include tapers, as shown in maximum gain surface wave antenna of Fig. 3.2. The implementation of tapers, progressive changes in the diameter of (3.56), introduces a layer of complexity that requires a more generalized approach to DRA design and reveals more about the relationships between physical dimensions and electrical performance than its non-tapered counterpart. Therefore, maximum gain surface wave antenna design is used here in the development of planar-fed, planar-fed arrays, and cladded DRAs.

As discussed in Chapter 2, the discontinuity radiation principle best predicts the radiation pattern of DRAs. This is also true of surface wave antennas. The total radiation pattern of the antenna is the result of the pattern from the feed in the absence of the surface wave antenna and the pattern at the terminal plane of the antenna. Eq. (3.60) is an approximate expression for the terminal radiation pattern, $T(\theta)$. The contribution to the far field pattern from the feed radiation depends on the type of feed used to excite the surface wave along the antenna. No matter what type of feed is used to excite the surface wave along the antenna, $T(\theta)$ dominates more or less on boresight depending on the distance between the feed plane and the terminal plane and the phase difference between them along the rod.

$$T(\theta) \approx \frac{1}{\frac{\lambda}{\lambda_z} - cos(\theta)} \tag{3.60}$$

$$k_z \cdot l - k_0 \cdot l = \phi \tag{3.61}$$

$$\frac{\lambda}{\lambda_z} = 1 + \frac{\phi \cdot \lambda}{2\pi \cdot l} \tag{3.62}$$

Eq. (3.61) represents the phase difference mentioned above and is rearranged in (3.62) to relate that phase difference to the field quantity of (3.57). In the design of maximum gain surface wave antennas, target values of phase, ϕ, for various lengths have been determined experimentally for maximum gain at those lengths as discussed in Chapter 4. The target phase value for a given length yields a corresponding value of $\frac{\lambda}{\lambda_z}$ in (3.62). That value may be used to predict the terminal pattern of (3.60) for the evaluation of the feed pattern or total radiation pattern. More importantly for the design of the antenna, the eigenvalues that satisfy (3.47) and (3.57) for the value of $\frac{\lambda}{\lambda_z}$ from (3.62) produce a unique diameter value in (3.56). The preceding logic and equations are valid for non-tapered rods, as in Fig. 3.3. Tapers are discussed in Chapters 4 and 5. The most efficient way to the phase difference contributed by tapers along the rod is to break the tapers up into step-wise, constant cross-section lengths and use the equations herein for each step.

Figure 3.3: Constant cross-section dielectric rod. As a DRA, this rod radiates at the feed and terminal ends. According to the discontinuity radiation principle, fields from both the feed and terminal planes contribute to the far-field radiation pattern.

The gain of a maximum gain surface wave antenna is (3.63). The half power (3 dB) beamwidth of the terminal pattern in a maximum gain surface wave antenna is (3.64). An approximation for the gain of a maximum gain surface wave antenna is (3.65).

$$Gain = \frac{10 \cdot l}{\lambda} \tag{3.63}$$

$$HPBW \approx 55 \cdot \sqrt{\frac{\lambda}{l}} \tag{3.64}$$

$$Gain \approx \frac{30,000}{HPBW^{\circ}_{E-plane} \cdot HPBW^{\circ}_{H-plane}} \tag{3.65}$$

For surface wave antennas, the ratio of total power to the input power is typically 65-75% [1]. Radiation efficiency can be very high, especially for DRAs as shown in Chapter 4. Dielectric and metallic losses are found mostly in the underlying feed.

One of the well-established benefits of surface wave antennas is broad bandwidth. Chapter 2 highlighted a study by Generalov et al. [48] that demonstrated using a single DRA across 900 GHz by changing the feed of the DRA. The impedance bandwidth, then, was a function of the match of the DRA to its hollow metallic waveguide feed and not necessarily limited by the DRA itself. The hollow metallic waveguide-fed DRA of Chapter 6 and the planar-fed DRA of Chapter 4 have impedance bandwidths that closely match the impedance bandwidths of the underlying feeds without the DRAs. DRA impedance bandwidth can be as broad as other surface wave antennas if the underlying feed impedance bandwidth does not limit its bandwidth.

Gain bandwidth may also be broad as with other surface wave antennas. However, in the case of the dielectric rod, dispersion becomes a factor at higher frequencies, as seen in Chapters 4, 5, and 6. The effect is less prominent in the cladded DRA presented here because these DRAs are made with a Rogers material with low dispersion in Ku-band. This is not the case for the 3D printed ABS rods used in the planar-fed and planar-fed array designs. The gain versus frequency plots for these antennas show dispersion begin to affect the gain bandwidth of the DRA above 15 GHz.

The polarization of the surface wave antenna depends on the cross-sectional dimensions of the DRA. However, the primary factor in polarization in the DRA is the polarization of the underlying feed. A circular cross-section DRA can accommodate any polarization, unless the underlying feed is linearly polarized. A rectangular cross-section DRA is linearly polarized with low cross-polarization if the height to width ratio of the cross-sectional dimensions are kept at 2:1 [8].

More details about the canonical design procedure and modifications to accomplish the design objectives at hand are given in the following chapters. However, a summary of Zucker's [1] maximum gain surface wave antenna design procedure is summarized below.

3.3 Design Methods for Maximum Gain DRAs

Zucker's [1] design method for maximum gain surface wave antennas is used as the starting place for the designs described in this work. References to surface wave features and dimensions are illustrated in Fig. 3.2. The canonical design procedure is summarized as follows:

1. Choose length for desired maximum gain. Length is the feed taper length and the constant diameter, or constant cross-section, length. The matching and terminal tapers are not included in the overall length of the DRA.

2. The diameter, d_2, is chosen to be the diameter necessary for a straight rod to achieve an optimal phase phase difference between the free space wave and the surface wave along the rod for a rod length. For rods between 3λ and 8λ in length, the optimal phase difference approaches 120°.

3. The feed of the straight rod is inefficient. A slow wave is launched more efficiently than a phase surface wave. Therefore, the recommendation by Zucker for launching a surface wave at the feed of a surface wave antenna is for the wavelength ratio to be between 1.2 and 1.3 at the feed point. This ensures a slow surface wave at the feed, which allows the surface wave to form along the rod and travel along the feed taper.

4. The feed taper length, l_{ft}, should be as short as possible. Tapers along the rod fill in the first nulls, broaden the main beam, and lower the gain of the antenna. Other than facilitating a more efficient feed and an improved match to free space at the rod termination, tapers are not are a detriment to rod gain. As rule of thumb for the length of the feed taper is to choose its length to be 20% of the total length of the rod. That length may be chosen as the length needed to achieve a desired gain or for other reasons, such as a maximum length that may be reliably printed by a 3D printer.

5. Since part of the length of the rod chosen to achieve the optimal phase difference over the length of the rod becomes the feed taper, the remaining length of the DRA maintains the constant length of diameter, d_2.

6. A terminal taper is added to the end of the DRA to match the surface wave to free space. The objective is to rapidly accelerate the surface wave to the velocity of the free space to reduce reflections back along the rod. The terminal taper begins at the end of the rod and ends in the diameter associated with $\frac{\lambda}{\lambda_z} = 1.0$. The length of the terminal taper is 1/2 λ.

Table 3.1: Maximum gain surface wave antenna design

Length	$n \cdot \lambda_0$
l_{ft}	$0.2 \cdot l$
l_{cd}	$0.8 \cdot l$
Gain	$\frac{10 \cdot l}{\lambda_0}$
Matching taper length	$\geq 1.5 \cdot \lambda_0$
l_{tt}	$0.5 \cdot \lambda_0$
$\frac{\lambda_0}{\lambda_z}$	$1 + \frac{\phi \cdot \lambda_0}{2\pi \cdot l}$
d_2	$60^\circ \leq \phi \leq 120^\circ$, over l

Chapter 4: Planar-fed Dielectric Rod Antenna Design

The DRA design method presented here is based on empirical observations and involves a series of steps for optimizing the phase difference between the travelling wave outside the rod and inside the rod to shape the radiation pattern according to the discontinuity radiation concept. The total phase difference, ϕ, over the length of a generic constant diameter dielectric rod, l_{rod}, is shown in (4.1) in terms of the free space and surface wave propagation constants. This relationship is expressed in (4.2) in terms of the free space wavelength, λ, and the surface wave wavelength, λ_z. The diameter of a constant diameter rod is calculated from the associated wavelength ratio of (4.2) using Fig. 2.1.

$$k_z \cdot l_{rod} - k \cdot l_{rod} = \phi \tag{4.1}$$

$$\frac{\lambda}{\lambda_z} = 1 + \frac{\lambda \cdot \phi}{2 \cdot \pi \cdot l_{rod}} \tag{4.2}$$

4.1 Design for Maximum Gain

The maximum theoretical gain of DRAs is determined by analogy to Yagi-Uda antennas, which are another type of surface wave antenna. For Yagi-Uda antennas with total length between 3λ and 8λ as measured from the beginning of the feed to the terminal plane, the gain is calculated by (4.3) [1, 72]. This expression of gain is feed dependent. In simulations of planar-fed DRAs of varying length, we have found (4.3) to be the maximum gain associated with the length of the constant diameter section of Fig. 4.1. In this case, (4.3) corresponds to the maximum gain for a constant diameter DRA between 3λ and 8λ in length assuming high excitation efficiency at the feed end and a good match to free space at the terminal end. A taper is added to the feed end of the rod to maximize excitation efficiency and to ensure a fully formed surface wave at the beginning of the constant diameter rod. Another taper is added to the terminal end of the constant diameter rod to match the surface wave to free space by rapidly increasing the surface wave velocity to match the free space wave velocity.

$$Gain = \frac{10 \cdot l_{rod}}{\lambda} \tag{4.3}$$

Ehrenspeck and Poehler [72] examined the optimal phase difference along Yagi-Uda antennas for maximum gain. They determined, for antennas between 4λ and 8λ in length, a phase difference at the end of the antenna of approximately 120° is optimal for maximum gain. This phase difference is ϕ in (4.1). For the planar-fed DRAs examined here, it has been found that the maximum gain of (4.3) is obtained when the 120° phase difference is approximately equally divided over l_{cd} and the feed taper. This finding is consistent with the minimum length required to ensure a fully formed surface wave by the end of the feed taper; the minimum length is one that will produce a 60° phase difference after a feed discontinuity [1]. There are two such discontinuities for the DRA designs studied here: the feed of the DRA corresponding to the beginning of the feed taper, and the end of the feed taper launching its surface wave onto the constant diameter section.

$$\frac{\lambda}{\lambda_z} = 1 + \frac{\lambda}{6 \cdot l_{cd}} \tag{4.4}$$

Our design procedure for a planar-fed DRA is a modified version of Zucker's design guidelines for surface wave antennas and is summarized as follows:

1. For a desired length of l_{cd}, the maximum gain is determined according to (4.3). Eq. (4.3) may also be used to determine the necessary value for l_{cd} to achieve a desired gain.

2. The diameter d_2 is calculated from the $\frac{\lambda}{\lambda_z}$ value from (4.4) using the desired value of l_{cd} and Fig. 2.1. This value of d_2 ensures a phase difference of 60° along l_{cd}.

3. For surface wave antennas the recommended value for $\frac{\lambda}{\lambda_z}$ at the feed is between 1.2 and 1.3. For a planar-fed DRA, the optimal value for d_1 at the feed found by optimization is the

diameter associated with $\frac{\lambda}{\lambda_z} = 1.3$, as determined from Fig. 2.1. If the initial diameter of the rod is too large, the incident wave travels within the rod and there is no surface wave. If the diameter is too small, the rod doesn't interact with the incident wave from the feed. The resulting diameter at the feed is larger and the surface wave is slower than at any other point along the rod.

4. The feed taper length is selected to be approximately 25% of l_{cd}, following recommendations based on empirical work for Yagi-Uda antennas in [1]. Full-wave simulations for the designs herein confirm that this provides the optimal gain, and a step-wise approximation of the phase contributed by the taper from d_1 to d_2 shows approximately 70 degrees of phase shift along l_{ft}. This is close to the value of 60 degrees mentioned above.

5. For best match of the radiating end of the DRA to free space, the phase velocity of the surface wave should be the same as that of free space: $\frac{\lambda}{\lambda_z} = 1$. This is accomplished by choosing the value of d_3 associated with $\frac{\lambda}{\lambda_z} = 1$ from Fig. 2.1. The terminal taper length, l_{tt}, is 0.5λ long.

Fig. 4.1 illustrates a planar-fed DRA designed using the above method. The resulting dimensions of a 15 GHz DRA design using this design method are outlined in Table 4.1. Table 4.2 summarizes the performance of the individual planar-fed DRA. The simulated DRA gain is within 0.3 dB of the theoretical gain. The simulations assume 100% infil ABS with $\varepsilon_r = 2.6$ and tan $\delta = 0.0052$. The substrate is 0.5 mm thick Rogers 4003 substrate, $\varepsilon_r = 3.55$ and tan $\delta = 0.0027$, with 17 um thick copper.

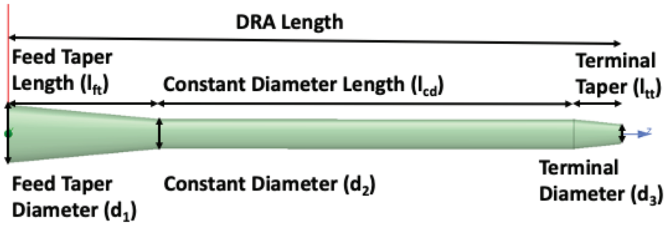

Figure 4.1: Maximum gain design for circular cross-section planar-fed DRA.

Table 4.1: Summary of DRA dimensions (*mm*)

Constant Diameter Length: l_{cd}	96
Feed Taper Length: l_{ft}	24
Terminal Taper Length: l_{tt}	10
Feed to Terminal Taper: $l_{ft} + l_{cd}$	120
Feed Diameter: d_1	12.4
Constant Diameter: d_2	6.8
Terminal Diameter: d_3	4.2

Table 4.2: Summary of DRA performance

Theoretical Gain (dBi), Eq. (4.3)	16.8
Simulated Gain (dBi)	16.5
Simulated 3dB Beamwidth (deg)	26
Simulated Sidelobe Level (dB)	-16

4.2 Efficient Excitation and the Planar Feed

By the discontinuity radiation concept, radiation occurs at discontinuities along the rod. The feed is one such discontinuity. The objective of feed design is maximum power transfer into the surface wave. However, since the feed is a discontinuity, there will be radiation. As detailed above, the radiation from the feed contributes to the final radiation pattern of the DRA.

Not much has been written about using a planar circuit structure as a feed for DRAs or, alternatively, using DRAs to enhance the performance of planar radiators. However, planar feeds have been successfully demonstrated [19, 22]. The planar feed is similar to the hollow metallic waveguide feed in that both have a radiating aperture. The surface of the planar radiator and the plane corresponding to the open termination of the metallic waveguide both present mode configurations similar to the dominant surface wave mode. Placing a DRA directly on a planar radiator is therefore conceptually similar to placing a DRA at the radiating aperture of an open metallic waveguide, although there are important differences.

The fundamental TE_{10} and TE_{11} mode in the hollow metallic rectangular and circular waveguides, respectively, are similar to the HE_{11} hybrid dominant mode in the circular cross-section

DRA. In the metallic waveguide-fed DRAs of Fig. 4.2, tapering the dielectric inside the metallic waveguide creates a gradual transition from the inside of the waveguide to the surface of the rod, which results in less reflection and more power available for both the surface wave and radiation from the feed.

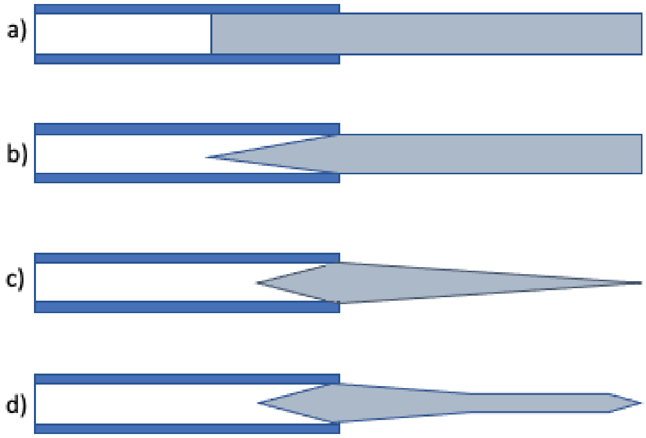

Figure 4.2: Examples of dielectric rod antennas with hollow waveguide feeds. a) Uniform DRA inserted into waveguide feed, b) uniform DRA with matching taper inserted into waveguide feed, c) continuous taper dielectric rod with matching taper inserted into waveguide, d) maximum gain DRA design according to [1]
.

The matching taper is not possible for planar DRA feeds. Matching the planar radiator feed to the DRA is accomplished by modelling the planar radiator as a conductor layer on a thin, high dielectric substrate backed by an infinite dielectric block of the same material as the DRA. Failure to include the infinite dielectric backing will result in a shift in the resonant frequency of the slot antenna when in contact with the DRA.

A folded dipole slot antenna is used here as the planar feed for each DRA in the 2 x 2 array. The DRA acts as a thick dielectric backing to the dipole slot substrate. The design of the folded dipole slot antenna, as with other patch and slot antennas, necessarily takes the material characteristics and thickness of the dielectric substrate into account. The radiator is designed for the effective dielectric constant of its substrate backed by an infinite slab of the DRA material.

A CPW is used to feed the folded dipole slot in order to present a balanced feed to the slot. The impedance of the folded dipole slot is high enough to be more easily matched to the planar

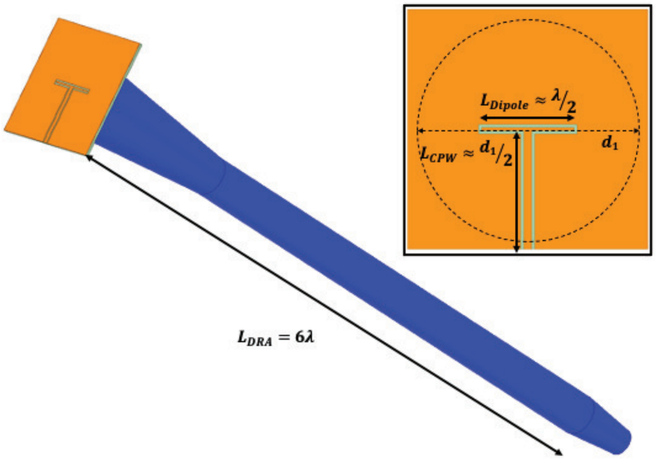

Figure 4.3: Folded dipole slot-fed DRA. The folded dipole slot antenna is fed by coplanar waveguide (CPW) (inset). The dotted circle illustrates the footprint of the DRA under the dipole-slot feed.

array feed with a 50 Ω input impedance. Simmons [73] gives detailed design procedures for CPW backed by an infinite dielectric substrate.

The thin substrate layer is 0.5 mm thick Rogers 4003C. The CPW feed is 6 mm long with a 0.254 mm gap width. The folded dipole slot is 7.72 mm long and 0.76 mm wide. The center spacing between the slots of the folded dipole is 0.252 mm wide. The feed dimensions of the rod are summarized in Table 5.1.

The simulated fields associated with the planar-fed DRA are shown in Figs. 4.4 and 4.5. Figs. 4.4a and 4.5a show the fields associated with the planar feed without the DRA from two different points of view. In these figures, the dipole pattern is clearly seen, radiating evenly in both directions away from the radiator. The effect of adding the DRA to the planar feed is seen in the field plots of Figs. 4.4b and 4.5b. In each case, the field tends toward the DRA, radiating predominately along the DRA axis. The beginning of the formation of a surface wave is most clearly seen at the boundary of the DRA in Fig. 4.5b.

4.3 Simulated Performance of the Planar-fed DRA

Fig. 4.6 compares the S_{11} of the folded dipole slot-fed DRA and a folded dipole slot backed by a half-spaced filled with the same material as the DRA. The S_{11} of the planar-fed DRA is that of a resonant planar dipole slot antenna. It has a single, deep resonance and the bandwidth of a dipole

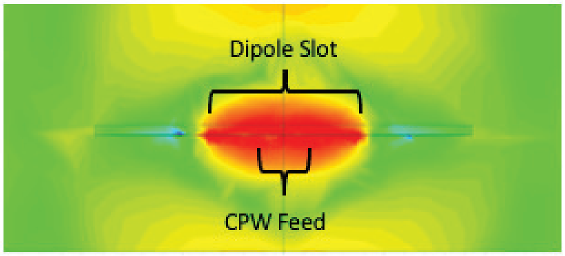

(a) E-field without DRA

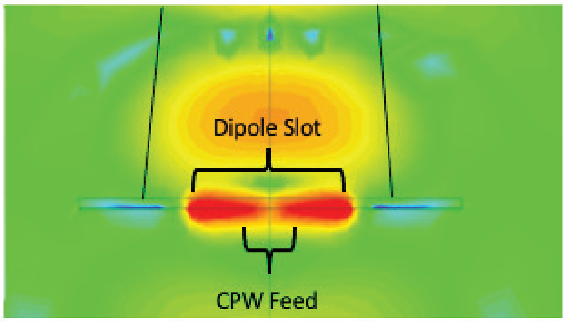

(b) E-field with DRA

Figure 4.4: Comparison of the electric field as seen from the CPW feed. The fields in the CPW feed and folded dipole slot are pictured with and without the DRA as seen from the CPW feed looking toward the DRA. The dipole pattern is visible in the a). The wave inside the DRA is visible in b).

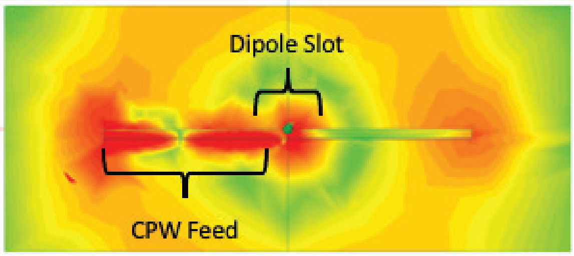

(a) E-field without DRA

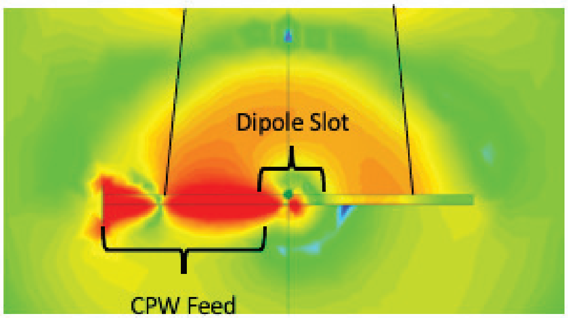

(b) E-field with DRA

Figure 4.5: Comparison of the electric field viewed normal to the CPW feed. Normal to the feed refers to the view along the folded dipole slot. The dipole pattern is seen in a). The beginning of the formation of the surface wave is seen in b).

slot. This is as expected since the design is fundamentally that of a dipole slot taking into account its unique substrate: that of the DRA.

Fig. 4.7 compares the simulated radiation efficiency of the DRA with a lossless substrate and conductor layer to the simulated radiation efficiency of the DRA with a lossy substrate and conductor layer. Losses in the feed have minimal impact on the radiation efficiency across the band. Even though DRAs are typically fed with rectangular waveguides, this shows the viability of planar-integrated DRAs. The radiation efficiency of the planar feed is greater than 90% from 12 GHz to 18 GHz. Losses in the substrate and conductor account for about 5% reduction in the radiation efficiency across the band. The reference plane for the single DRA simulations is shown in Fig. 5.2.

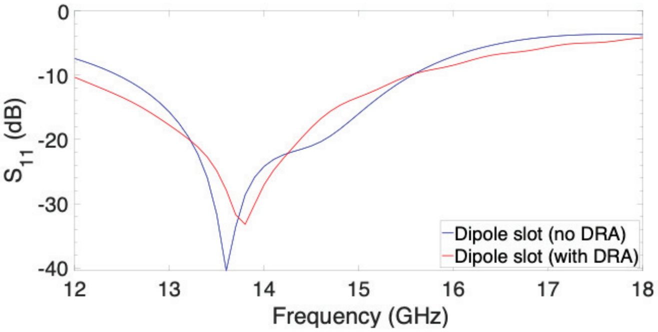

Figure 4.6: Simulated S_{11} of a planar folded dipole slot-fed DRA. This feed is compared to the same feed without the DRA. For the feed without the DRA, the substrate of the folded dipole slot is backed by an infinite block of the same material as the DRA.

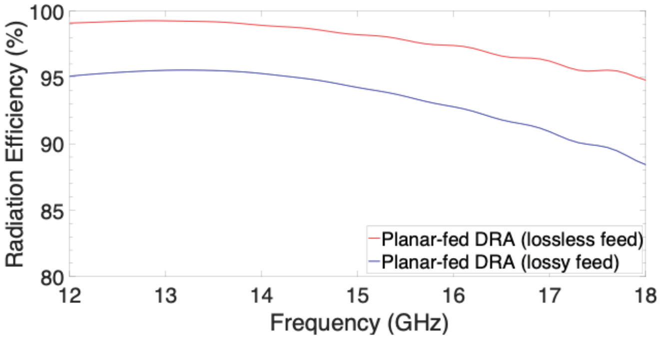

Figure 4.7: Comparison of simulated DRA radiation efficiencies. Efficiencies of the planar-fed DRA with a lossy substrate and conductor are compared to the same DRA with a lossless substrate and conductor. The DRA material is lossy in both cases.

Chapter 5: Planar-fed Dielectric Rod Antenna Array

This paper presents the design and performance of a 2 x 2 array of 3D printed cylindrical dielectric rod antennas that is integrated with a planar feed network. The array does not use metallic waveguide as part of the feed mechanism or support for the dielectric rod. The resulting design is an efficient, low-cost, scalable implementation of a high gain Ku band array.

5.1 DRA Array Design

For an array of DRAs with limited mutual impedance, the maximum theoretical gain is that of a surface wave antenna array. The spacing between the elements influences the gain of the array. In order to approach this maximum theoretical gain, the spacing between the centers of the individual elements, d_s, is chosen according to the approximation of (5.1) [1], where l is the DRA length and λ is the free space wavelength. The lower limit of (5.1) is a minimum spacing guideline to maintain mutual coupling between elements of at most $-10\ dB$. The upper spacing limit of (5.1) maximizes attenuation in the first principle sidelobe. Pattern multiplication of the individual element pattern and the underlying array factor results in an increase in the array pattern gain on boresight as shown in Fig. 5.1. The main lobe of the elements is narrowed by the deep nulls in the array factor nearer to boresight than in the element pattern.

$$0.5\sqrt{\frac{l}{\lambda}} \leq \frac{d_s}{\lambda} \leq \sqrt{\frac{l}{\lambda}} \tag{5.1}$$

Following these element spacing guidelines, the spacing for 6λ long planar-fed DRAs at 15 GHz should be between 24.5 mm and 49.0 mm. Optimizing the gain in simulation resulted in 52 mm spacing for maximum gain in the array. This is a slightly larger spacing than what is estimated by (5.1).

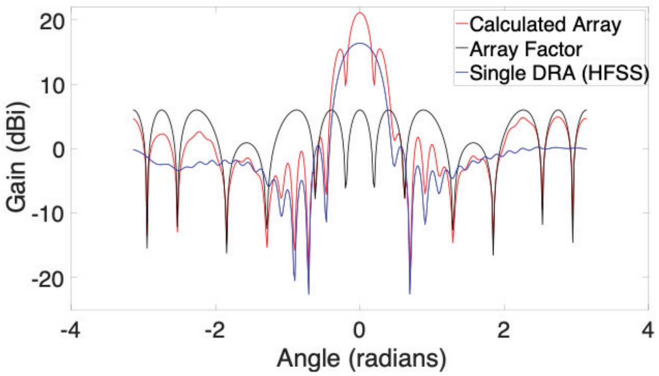

Figure 5.1: Calculated radiation pattern for the 2 x 2 DRA array. The array factor is multiplied with the simulated individual element pattern to produce the theoretical array radiation pattern.

The folded dipole slot is fed by the CPW feed of length L_{CPW} (Fig. 5.2). The three line coupler represented by the W1, W2, and W3 in Fig. 5.2 transitions the grounded microstrip feed into the ungrounded CPW dipole slot feed. The microstrip to coplanar waveguide transition is as described in [73]. Ungrounded CPW is chosen to allow the radiation from the dipole slot antenna to travel to the dielectric rod without interference from a nearby ground plane. This transition section at each of the four dipole slots makes the corporate, grounded microstrip array feed of Fig. 5.3 possible.

The rest of the array feed is a grounded microstrip corporate feed as in Figs. 5.3 and 5.4. The ground layer only runs beneath the microstrip feed and the individual three-line coupler transition sections and is annotated in Fig. 5.4. The dimensions of the planar array feed are listed in Table 5.1. The array of folded dipole slots are excited simultaneously, in phase, from a single 50 Ω input. The 50 Ω array input impedance is transformed to 25 Ω by a quarter-wave impedance transformer before the first 3 *dB* power divider, resulting in two 50 Ω microstrip lines. These two 50 Ω microstrip lines are divided again by two respective 3 *dB* power dividers, resulting in a phase-aligned 100 Ω input to each of the four folded dipole slots.

5.2 Fabrication

The planar antenna and array feed are built on 0.508 mm thick Rogers 4003C with a dielectric constant $\varepsilon_r = 3.55$. The circular cross-section dielectric rods are printed using the fused deposition modelling technique with 100% infil ABS plastic with $\varepsilon_r = 2.6$ and a 0.0052 dielectric loss tangent.

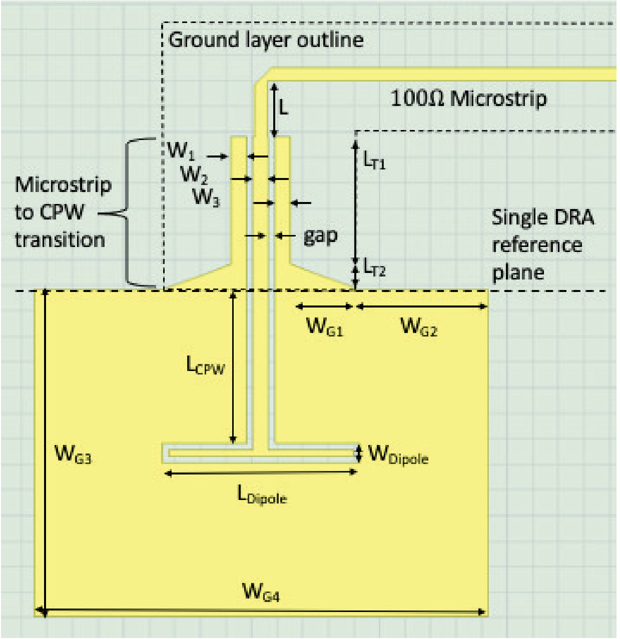

Figure 5.2: Single antenna array element. Folded dipole slot fed by a 100 Ω microstrip line. The microstrip to CPW transition converts the fields in the grounded microstrip line into the ungrounded CPW feed, which is a balanced feed for the folded dipole slot antenna. The ground layer of Fig. 5.4 is represented by the dotted outline. The reference plane of the single DRA of Chapter 4 is marked.

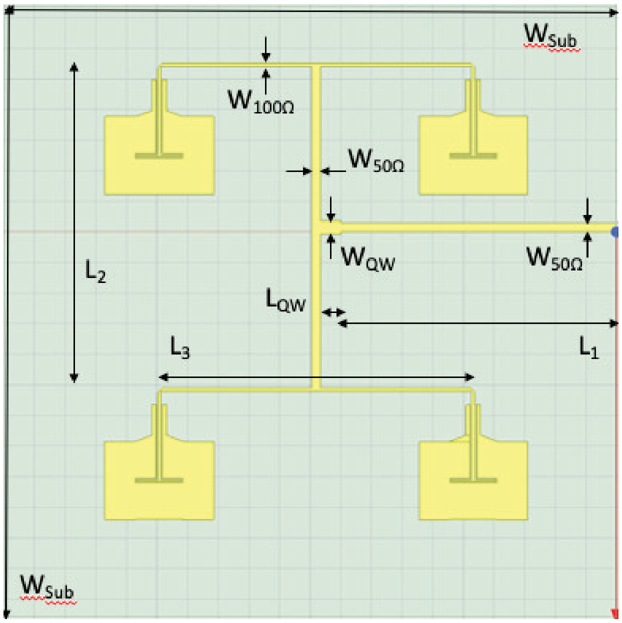

Figure 5.3: The four-element folded dipole slot array and feed network. The 50 Ω input impedance feeds four individual 100 Ω inputs using a quarter wave transformer and three 3 *dB* power dividers.

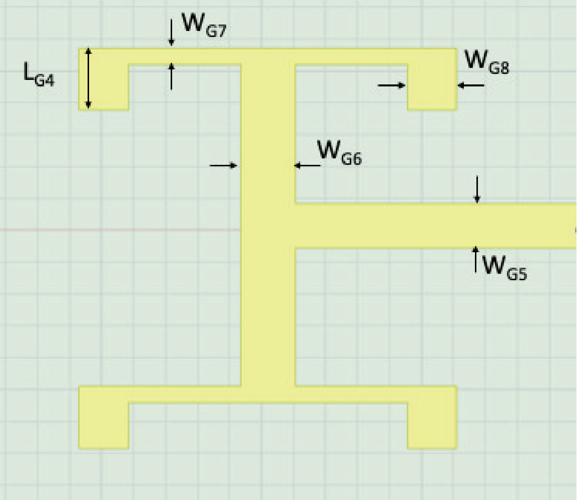

Figure 5.4: Array ground trace. This layer is on the opposite side of the substrate from Fig. 5.3.

Table 5.1: Summary of array feed dimensions (*mm*)

L	2.19	$\mathbf{L}_{T1}$	5	$\mathbf{L}_{T2}$	1
$\mathbf{W}_1$	0.6	$\mathbf{W}_2$	0.6	$\mathbf{W}_3$	0.6
gap	0.254	$\mathbf{W}_{G1}$	2.7	$\mathbf{W}_{G2}$	5
$\mathbf{W}_{G3}$	12.79	$\mathbf{W}_{G4}$	17.72	$\mathbf{L}_{CPW}$	6
$\mathbf{W}_{Dipole}$	0.76	$\mathbf{L}_{Dipole}$	7.72	$\mathbf{W}_{Sub}$	100
$\mathbf{L}_1$	45	$\mathbf{L}_2$	52.55	$\mathbf{L}_3$	50.77
$\mathbf{W}_{QW}$	3.3	$\mathbf{L}_{QW}$	2.28	$\mathbf{W}_{50\,\Omega}$	1.39
$\mathbf{W}_{100\,\Omega}$	0.5	$\mathbf{L}_{G4}$	9.69	$\mathbf{W}_{G5}$	6.95
$\mathbf{W}_{G6}$	8.5	$\mathbf{W}_{G7}$	2.5	$\mathbf{W}_{G8}$	7.72

The diameter d_2 of the fabricated rod used in the array design is 6.68mm, which is slightly smaller than the value listed in Table 4.1. This minor difference did not significantly change the simulated performance of the individual DRA.

Each rod is 6λ long at 15 GHz, 120 mm, plus the added length of the Terminal Taper of Fig. 4.1, 10 mm, for a total length of 130 mm. At 130 mm length, these rods were approaching the z-axis height limit of many 3D printers. Without a sturdy printed base, the rods begin to physically oscillate, destroying the consistency of the print toward the end of the rod. Longer 3D printed rods, though desirable for higher gain, may not be easily printed with desktop 3D printers.

The Rogers 4003C was milled using standard PCB milling techniques. The DRAs were 3D printed vertically from the feed on the printer plate upward to the end of the terminal taper. The individual DRAs were glued to the substrate side of each dipole slot by hand. The final array is shown in a near field range at NSI-MI in Suwanee, GA in Fig. 5.5.

5.3 Performance: Simulation vs Measurement

The individual element gain simulated in HFSS is 16.5 *dBi*. According to (5.2), the theoretical array gain for this 4 element array is 22 *dBi*. When calculated from array theory by pattern multiplication of the simulated individual element pattern with the array factor, the gain is 21 *dBi*.

$$ArrayGain = n \cdot Gain_{Element} = n \cdot \frac{10 \cdot l_{cd}}{\lambda} \tag{5.2}$$

Antenna measurements were taken at NSI-MI and the Georgia Institute of Technology. The simulated and measured S_{11} are compared in Fig. 5.6. The measured S_{11} shows good agreement to simulation. The simulated, calculated, and measured array patterns are compared in Fig. 5.7. The simulated and measured patterns show good agreement. The measured gain is 19 *dBi*, which is 0.3 *dB* below the simulated gain of 19.3 *dBi*. Both simulated and measured patterns have a 3 *dB* beamwidth of 8 degrees with the first sidelobes 10 *dB* below the gain of the main lobe. The 3 *dB* gain bandwidth of the array is 26% (Fig. 5.8) and the radiation efficiency of the array at 15 GHz is 80%, as in Fig. 5.9.

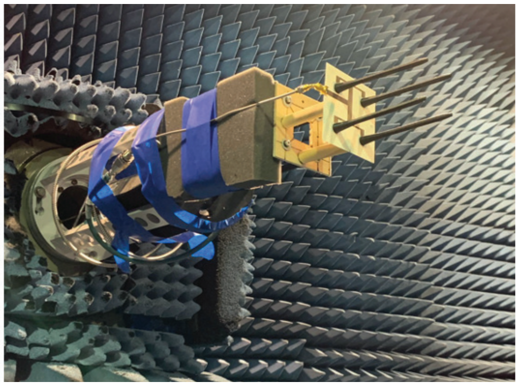

Figure 5.5: Array test setup at NSI-MI, Suwanee, GA

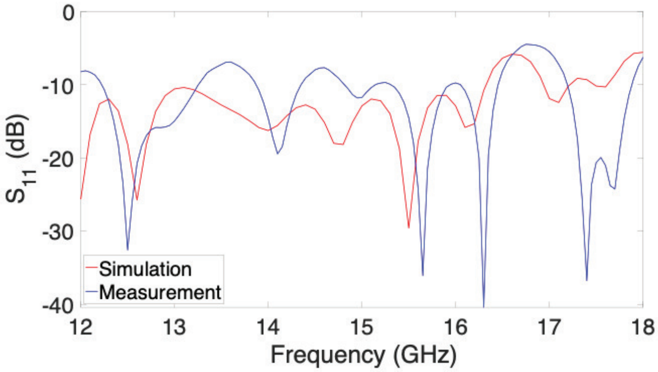

Figure 5.6: Simulated array S_{11} compared to measured array S_{11}.

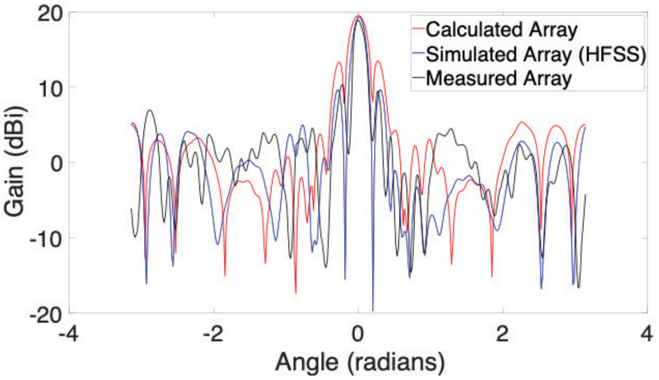

Figure 5.7: DRA array radiation pattern. Comparison of the calculated, simulated, and measured DRA array radiation patterns at 15 GHz.

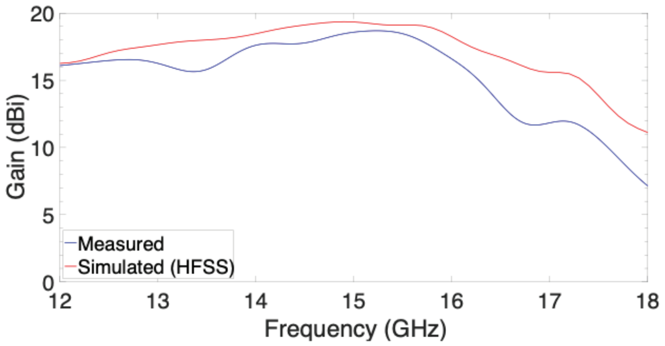

Figure 5.8: Comparison of simulated and measured array gain versus frequency.

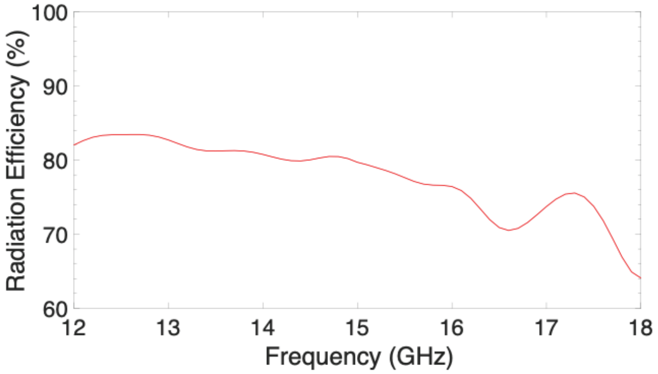

Figure 5.9: Simulated array radiation efficiency.

5.4 Conclusions

A fabricated 2 x 2 array of folded dipole slot antenna fed DRAs achieves a gain 19 *dBi* with a 3 *dB* gain bandwidth of 26%. The 4-element array is simple, cost-effective to fabricate, being made with standard PCB processes and 3D printed ABS plastic DRAs, and may be scaled into the mm-wave regime. Future iterations of this design may take advantage of earlier work in cladded dielectric rod antennas [8] to further customize the size, footprint, weight, and robustness of the array by printing high dielectric constant rods embedded in lower dielectric, 3D printed cladding.

Chapter 6: Design of Cladded Dielectric Rod Antennas[1]

A dielectric rod antenna is designed in Ku-band using established principles for designing maximum gain surface wave antennas in free space as in [1]. The design principles are modified to their most general form and applied to the design of three dielectric rod antennas embedded in a dielectric cladding of different dielectric constant: $\varepsilon_r = 1.0$ (free space ”cladding”), $\varepsilon_r = 1.6$ (3D printed ABS with 50% in-fill), and $\varepsilon_r = 2.6$ (3D printed ABS with 100% in-fill). The antennas are simulated and measured to determine agreement between them and thereby validate the design procedure.

6.1 Introduction

Antenna selection typically involves consideration for size, weight, cost, and orientation relative to the system into which the antenna will be integrated, in addition to electromagnetic performance parameters such as gain, beamwidth, bandwidth, etc. Dielectric rod antennas (DRAs) offer advantages in weight and cost over their moderate-gain counterparts, and possibly also in ease of integration as the ability to 3D print these antennas improves.

Adding dielectric cladding to an uncladded DRA has been shown to improve gain. In [16], the DRA is designed to operate with cladding and the cladding is removed to observe changes in performance. The DRAs in both cases were the same. The DRA is designed according to [5] and [74] and optimized in simulation with Ansys High Frequency Structure Simulator (HFSS). Examples of other approaches to uncladded DRA design include [1, 3, 27, 51, 75, 76, 49, 77].

The design procedure that follows is for designing a rectangular waveguide-fed DRA for maximum gain taking into account the material immediately surrounding the DRA. This is the first

---

[1] This chapter was published by IEEE as G. L. Saffold and T. M. Weller, ”Design of Cladded Dielectric Rod Antennas,” 2019 IEEE 20th Wireless and Microwave Technology Conference (WAMICON), Cocoa Beach, FL, USA, 2019, pp. 1-4, doi: 10.1109/WAMICON.2019.8765464. Permission is included in Appendix A.

publication known to the author to provide a design methodology specifically for cladded DRAs. However, it is shown to be applicable to the design of uncladded DRAs by viewing the lack of cladding as a cladding with $\varepsilon_r = 1.0$. The methodology is based on the guidelines for designing maximum gain surface wave antennas, as presented by Zucker [1]. The design procedure is validated by the agreement in gain and beamwidth performance of the three antennas of different dimensions based on the choices of different cladding material.

6.2 Maximum Gain DRA Design

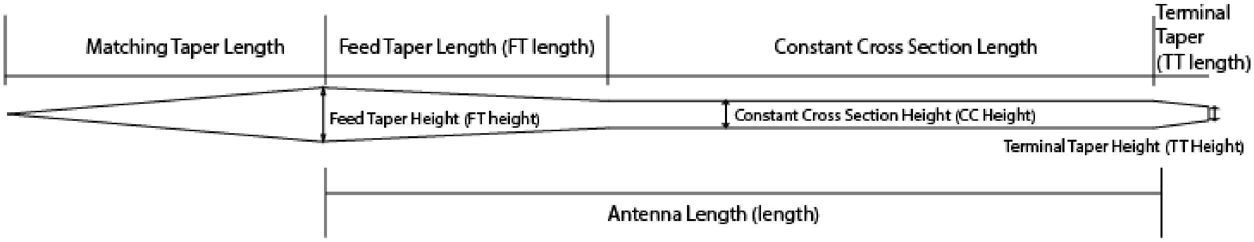

Figure 6.1: Rectangular waveguide-fed, rectangular cross-section dielectric rod antenna

The total pattern of the surface wave antenna may be evaluated as the superposition of two waves at the terminal aperture, which in the DRA is the end of the constant cross-section section and the beginning of the Terminal Taper of Fig. 6.1. One wave is the surface wave traveling along the antenna. The other is the wave radiated by the open end of the rectangular waveguide feed that is not converted into the surface wave [1][78].

In the design of maximum gain surface wave antennas, optimal target values for the phase difference between these two waves at different points along the antenna drive the determination of the dimensions of the antenna at those points. These phase differences may be algebraically rearranged in terms of the ratio of the wavelength in the cladding, λ_{clad}, and the wavelength of the surface wave traveling along the surface of the antenna, λ_{rod}.

Fig. 6.4 shows the relationship between $\frac{\lambda_{clad}}{\lambda_{rod}}$ and the rod diameter, d, for cylindrical dielectric rods fabricated with Rogers 3010, $\varepsilon_r = 10.2$, and cladding with dielectric constants of 1.0 for the uncladded rod, 1.6 for 50% in-fill ABS, and 2.6 for 100% in-fill ABS. These values for $\frac{\lambda_{clad}}{\lambda_{rod}}$ were calculated based on the fields in these dielectric rods following a publication by Elsasser [64] as a guide.

For each given combination of dielectrics, rod and cladding, values for the cylindrical rod diameter were calculated for values of the phase difference between the waves as represented by $\frac{\lambda_{clad}}{\lambda_{rod}}$, Elsasser's 'U' [64]. Cross-sectional area of the rectangular cross-section DRA is approximated from the calculated diameter by [1]:

$$A = \left(\frac{d}{1.13}\right)^2. \tag{6.1}$$

The points of different cross-sectional area along the DRA are linked by tapered sections of variable length. The tapers in the following DRA design are in the E-plane, along the short length of the cross-section of the rectangular waveguide feed. E-plane tapers have lower insertion loss vs H-plane tapers [74] and are used in this design. In order to maintain the E-plane taper, the thickness of the DRA is held constant. The tapers are a result of changes only in height along the rod.

The maximum gain of a surface wave antenna with perfect excitation of the surface wave may be approximated by [1]:

$$G = \frac{(10 * l)}{\lambda_{clad}}, \tag{6.2}$$

where l is the electrical length in terms of λ_{clad} and

$$\lambda_{clad} = \frac{\lambda}{\sqrt{\varepsilon_{clad}}}, \tag{6.3}$$

where λ is the free space wavelength, $\frac{c}{f}$. A desired maximum gain of 19 dBi corresponds to an electrical length of $8\lambda_{clad}$ from (6.2), which is the electrical length of each of the following DRAs.

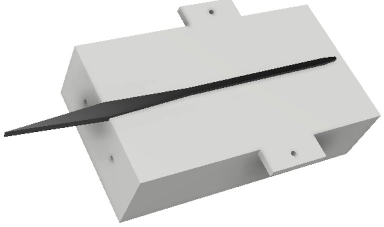

Figure 6.2: Cross-sectional view of DRA cladding with full DRA inside

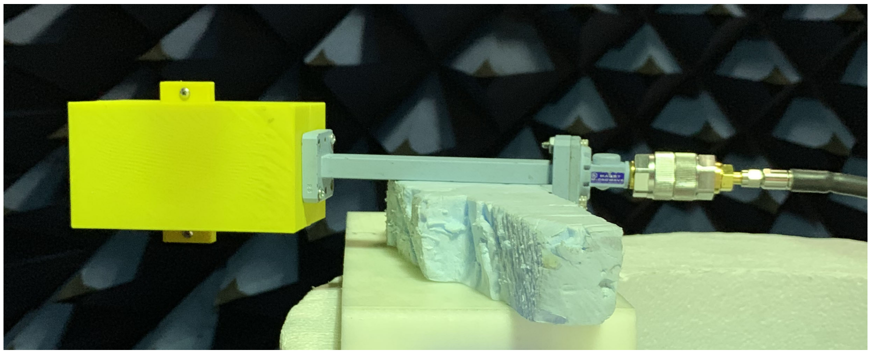

Figure 6.3: Cladded DRA fed by rectangular waveguide during test

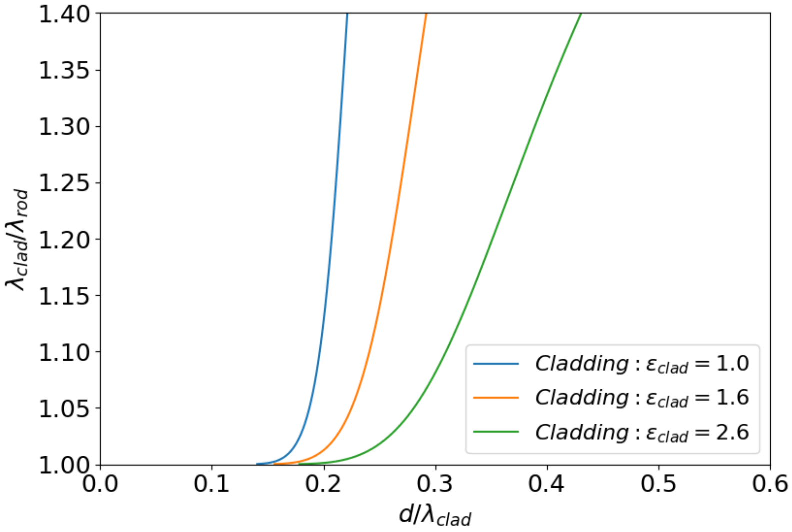

Figure 6.4: $\lambda_{clad}/\lambda_{rod}$ versus d/λ_{clad} for uncladded and cladded DRA

6.2.1 Matching Taper

A taper is inserted into the rectangular waveguide feed to reduce reflection of the guided wave within the rectangular waveguide resulting from the introduction of the dielectric rod at the open end of the rectangular waveguide. A target S_{11}, referenced to the feed end of the rectangular waveguide, is chosen to be -15 dBi or lower across the band. A matching taper length of $3\lambda_{clad}$ was found to be sufficient. The length of the matching taper has not been optimized.

6.2.2 Thickness and Feed Height

Beginning at the Feed Taper, Fig. 6.1, the surface wave must be efficiently launched onto the dielectric rod. The surface wave is most efficiently launched when [1]

$$1.2 < \frac{\lambda_{clad}}{\lambda_{rod}} < 1.3. \tag{6.4}$$

The cross-sectional area at the feed is determined by (6.4) and (6.1), following the procedure outlined in Section 6.2. The DRA thickness is then chosen such that the product of the thickness and a height of twice the thickness equals the desired cross-sectional area:

$$thickness = \sqrt{\frac{A}{2}}. \tag{6.5}$$

The thickness is the shortest cross-sectional dimension of the DRA and is parallel to the longest cross-sectional dimension of the rectangular waveguide.

This 2-to-1 height-to-thickness ratio is recommended at the feed of a rectangular dielectric rod in order to minimize cross-polarization in the DRA [79]. Therefore, the height at the feed is twice the thickness of the rod.

The feed taper length is optimized for maximum gain through simulation after all other parameters have been determined. The recommended length is greater than 1.5 λ_0.

6.2.3 Constant Cross-section Height

For maximum gain of a particular electrical length of antenna with 100% efficiency of surface wave excitation, $\frac{\lambda_{clad}}{\lambda_{rod}}$ at the end of the antenna length, Fig. 6.1, is

$$\frac{\lambda_{clad}}{\lambda_{rod}} = 1 + \frac{\lambda_{clad}}{6l}, \tag{6.6}$$

which results in a target value for $\frac{\lambda_{clad}}{\lambda_{rod}}$ from which to determine the desired cross-sectional area at the end of the antenna. Since the thickness of the antenna is constant and determined by the feed design, the height at the end of the antenna is determined by

$$height = \frac{A}{thickness}. \tag{6.7}$$

The cross-sectional area and height at the end of the antenna begins at the end of the Feed Taper. This results in a segment of the antenna with constant-cross section and height which begins at the end of the Feed Taper and ends at the end of the antenna, as in Fig. 6.1.

6.2.4 Terminal Taper

The Terminal Taper of Fig. 6.1 minimizes reflections at the end of the antenna by matching the surface wave to the surrounding medium. Zucker recommends a terminal taper length of 0.5λ ending abruptly with a cross-sectional area associated with $\frac{\lambda_{clad}}{\lambda_{rod}} = 1.0$. The Terminal Taper lengths used for the cladded antennas are $0.5\lambda_{clad}$. The terminal taper begins with the same height as the end of the antenna, tapers down over a distance of $0.5\lambda_{clad}$ to the height required for a cross-sectional area associated with $\frac{\lambda_{clad}}{\lambda_{rod}} = 1.0$.

6.2.5 Feed Taper Length

Finally, the Feed Taper must be at least long enough for the surface wave to be fully developed, allowing the remaining length of the antenna to be used to bring the phase difference between the surface wave and the wave from the feed to its optimal value, as in (6.6). Zucker suggests the minimum length of the Feed Taper occurs where the phase difference between the surface wave and the unguided wave from the feed reaches 180°: $\frac{\lambda_{clad}}{\lambda_{rod}} = 1 + \frac{\lambda_{clad}}{2l}$ [1].

The Feed Taper length is optimized in simulation for maximum gain using Zucker's approximate target of 180° phase difference as a starting point. In each case presented here, the Feed Taper length did not correspond to the recommended length associated with a 180° phase difference.

6.3 Measurement and Simulation Results

Table 6.1: Summary of DRA dimensions at 15 GHz (*mm*)

Cladding dielectric	$\varepsilon_{clad} = 1.0$	$\varepsilon_{clad} = 1.6$	$\varepsilon_{clad} = 2.6$
Length	160	126.5	99.2
Cross-sectional area (mm^2)	14.5	15.0	18.2
Thickness	2.7	2.7	3.0
FT height	5.4	5.5	6.0
FT length	20	80	34
CC height	3.6	3.1	2.5
TT length	10	7.9	6.2
TT height	2.3	1.7	1.3

The design procedure above was validated by designing three different DRAs. Each antenna was designed as described above using Rogers 3010, $\varepsilon_r = 10.2$, with no cladding ($\varepsilon_{clad} = 1.0$), ABS cladding with 50% infill ($\varepsilon_{clad} = 1.6$), and ABS cladding with 100% infill ($\varepsilon_{clad} = 2.6$). The dielectric cladding was chosen to be a 60 mm x 60 mm block centered on the DRA and extending 0.5λ beyond the end of the Terminal Taper of Fig. 6.1. The rest of the design parameters are summarized in Table 6.1.

Table 6.2: Summary of DRA Performance at 15 GHz

Cladding dielectric	**Gain (dBi)**	**HPBW**	**SLL (dB)**
$\varepsilon_{clad} = 1.0$ Sim	16.3	18°	-14
$\varepsilon_{clad} = 1.0$ Meas	15.7	21°	-8.5
$\varepsilon_{clad} = 1.6$ Sim	16.6	20°	-18
$\varepsilon_{clad} = 1.6$ Meas	18.5	16°	-14.5
$\varepsilon_{clad} = 2.6$ Sim	16.2	20°	-15
$\varepsilon_{clad} = 2.6$ Meas	15.7	16°	-8

Table 6.1 summarizes the relevant dimensions produced by following the design procedure. In general, the higher the ε_{clad}, the more compact the antenna, as expected. However, antenna thickness increased with increasing ε_{clad}. In addition, while the $3\lambda_{clad}$ Matching Taper length was produced a sufficient S_{11}, it may not have been the best choice for length. The Matching Taper is not surrounded by cladding. An optimized length based on λ may prove to be a better approach.

Fig. 6.5 shows the simulated patterns for all three DRAs. To validate the design procedure for cladded DRAs, the three antennas were specifically designed for the same target performance using the same material for the DRA and different cladding materials. The good agreement between the simulated performance of these antennas suggests that the procedure is valid.

Table 6.2 and Fig. 6.6 give the measured and simulated performance and patterns of the three DRAs. The good agreement in simulation extends to the measurements, with a notable exception. The measured Gain of the $\varepsilon_{clad} = 1.6$ DRA is 2 dBi higher than the simulation, which is closer to the theoretical maximum gain of (6.2). This discrepancy is best explained by possible variability in the dielectric constant of 50% infill ABS.

6.4 Conclusion

A novel design procedure for rectangular waveguide fed cladded dielectric rod antennas is presented here. This is the first procedure known to the authors specifically for the design of cladded DRAs. The procedure allows for differences in DRA as well as cladding material.

The good match between measurement and simulation suggests that the design methodology presented here is valid for designing maximum gain DRAs with and without cladding. However, rectangular waveguide-fed rectangular cross-section DRAs have been designed with higher gain than those presented in [16] which suggests the target values for $\frac{\lambda_{clad}}{\lambda_{rod}}$ may be different for DRAs than for generic surface wave antennas, as expressed in [1].

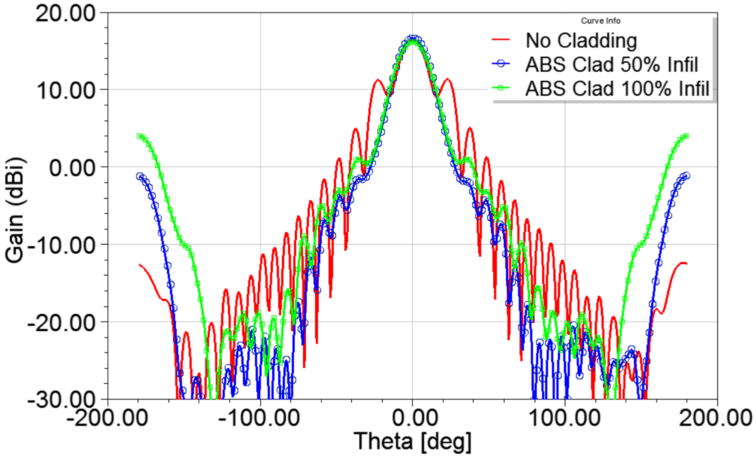

Figure 6.5: Simulated pattern comparison for all three DRAs: Total Gain (dBi) vs Theta (degrees)

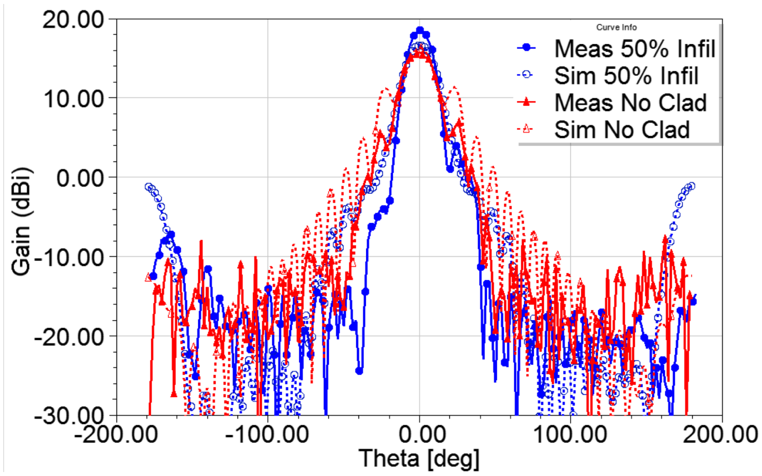

Figure 6.6: Simulated versus measured pattern for DRA with 50% infill ABS cladding and DRA without cladding: Total Gain (dBi) vs Theta (degrees)

Chapter 7: Recommendations and Future Work

1. W-band, cladded DRA array integrated with additive manufactured T/R Module. The ultimate objective of this project is to bring the work outlined here up to w-band direct integration into an additive manufactured T/R module for point-to-point communications.

2. Planar-fed DRA array in cladding at Ku-band for increased gain, reduced size, mechanical stability, and element alignment. The purpose of adding the cladding is to either increase the gain of the existing antenna design, reduce the size for the same gain, or reduce the size and increase the gain. Since alignment is difficult in the planar-fed array and radome integration is standard practice in antenna design, a useful follow-on extension of this work would be to 3D print a planar-fed DRA array in a block of lower dielectric cladding. The objective would be to increase the gain above the 20 dBi threshold while also encasing the DRAs in a protective layer with fixed, stable alignment.

3. Simplified algebraic DRA design procedure based on linear assumptions: avoid solving transcendental equations. It is possible to represent the $\frac{\lambda}{\lambda_z}$ versus $\frac{d}{\lambda}$ curves as straight lines for given materials. Moreover, a relationship between diameter and ε_r for a target value of $\frac{\lambda}{\lambda_z}$ exists which may form the basis for linear design curves and approximate algebraic relationships between diameter and target values of phase along strategic points along the rod. The object here is to create a more readily available design procedure that doesn't require graduate level math or expensive full wave simulation software.

4. Cross-sectional area equivalence between circular and rectangular cross-section DRAs. The lengths of the feed tapers in the maximum gain cladded DRAs do not follow the recommended lengths as closely as the circular cross-section DRAs, planar and waveguide-fed,

do. This suggests that the simplified conversion equation found in Chapter 6 may not be accurate or at least may be improved. Calculating the fields in rectangular cross-section dielectric rods is not as straight forward as it is for circular cross-section DRAs. It is worth examining this equivalence to either further validate it or improve and replace it.

References

[1] Francis J. Zucker. “Surface Wave Antennas”. In: *Antenna Engineering Handbook, Fourth Edition*. 2007, pp. 10–1 – 10–32. ISBN: 0071475745. DOI: 10.1036/0071475745. URL: http://mhebooklibrary.com/doi/book/10.1036/0071475745.

[2] Sergei P. Skobelev. *Phased Array Antennas with Optimized Element Patterns*. Norwood, MA: Artech House, 2011, p. 255. ISBN: 139781608071906.

[3] G. E. Mueller and W A Tyrrell. “Polyrod Antennas”. In: *Bell System Technical Journal* 26.4 (1947), pp. 837–851. ISSN: 15387305. DOI: 10.1002/j.1538-7305.1947.tb01324.x.

[4] Chandrakanta Kumar, V. Senthil Kumar, and V. V. Srinivasan. “Design aspects of a compact dual band feed using dielectric rod antennas with multiple element monopulse tracking”. In: *IEEE Transactions on Antennas and Propagation* 61.10 (2013), pp. 4926–4932. ISSN: 0018926X. DOI: 10.1109/TAP.2013.2271312.

[5] Jing-hui Qiu and Nan-nan Wang. “Optimized Dielectric Rod Antenna for Millimeter Wave FPA Imaging System”. In: *Imaging Systems and Techniques* (2009), pp. 147–150. DOI: 10.1109/IST.2009.5071621.

[6] Robab Kazemi, Aly E. Fathy, and Ramezan Ali Sadeghzadeh. “Dielectric rod antenna array with substrate integrated waveguide planar feed network for wideband applications”. In: *IEEE Transactions on Antennas and Propagation* 60.3 (2012), pp. 1312–1319. ISSN: 0018926X. DOI: 10.1109/TAP.2011.2182489.

[7] M. W. Rousstia and M. H.A.J. Herben. “60-GHz wideband branchline coupler and patch antenna with dielectric rod for full-duplex gigabit wireless communication”. In: *8th European Conference on Antennas and Propagation, EuCAP 2014* EuCAP (2014), pp. 201–205. DOI: 10.1109/EuCAP.2014.6901726.

[8] Gabriel L. Saffold and Thomas M. Weller. “Design of Cladded Dielectric Rod Antennas”. In: *2019 IEEE 20th Wireless and Microwave Technology Conference, WAMICON 2019*. 2019. ISBN: 9781538695975. DOI: 10.1109/WAMICON.2019.8765464.

[9] Denise C Lugo et al. “Ku band Metal-Strip-Loaded Dielectric Rod Antenna with Narrowband Gain Enhancement”. In: (2018), pp. 1889–1890.

[10] Jürgen Richter and Lorenz Peter Schmidt. “Dielectric rod antennas as optimized feed elements for focal plane arrays”. In: *IEEE Antennas and Propagation Society, AP-S International Symposium (Digest)* 3 A (2005), pp. 667–670. ISSN: 15223965. DOI: 10.1109/APS.2005.1552342.

[11] a. a. Generalov, D. V. Lioubtchenko, and a. V. Räisänen. “Dielectric rod waveguide antenna for 220-325 GHz”. In: *Proceedings of 6th European Conference on Antennas and Propagation, EuCAP 2012* (2012), pp. 3551–3553. DOI: 10.1109/EuCAP.2012.6205968.

[12] S. Kobayashi et al. *Dielectric Antennas for Millimeter-Wave Applications*. Tech. rep. Urbana: University of Illinois, 1980, pp. 566–569.

[13] S. Kobayashi, R. Mittra, and R. Lampe. "Dielectric tapered rod antennas for millimeter-wave applications". In: *IEEE Transactions on Antennas and Propagation* 30.1 (1982). ISSN: 0096-1973. DOI: 10.1109/TAP.1982.1142758. URL: http://ieeexplore.ieee.org/lpdocs/epic03/wrapper.htm?arnumber=1142758.

[14] T. Ando, J. Yamauchi, and H. Nakano. "Rectangular dielectric-rod fed by metallic waveguide". In: *IEE Proceedings - Microwaves, Antennas and Propagation* 149.2 (2002), p. 92. ISSN: 13502417. DOI: 10.1049/ip-map:20020264.

[15] L.W. Mickey and G.G. Chadwick. "Closely Spaced High Dielectric Constant Polyrod Arrays". In: *IRE International Convention Record* 1 (1958), p. 213. DOI: 1150685.

[16] Denise C. Lugo et al. "3D printed multilayer mm-wave dielectric rod antenna with enhanced gain". In: *2017 IEEE Antennas and Propagation Society International Symposium, Proceedings* 2017-Janua (2017), pp. 1247–1248. DOI: 10.1109/APUSNCURSINRSM.2017.8072666.

[17] J. P. Pousi et al. "High permittivity dielectric ROD waveguide antenna for 110-150 GHz". In: *European Space Agency, (Special Publication) ESA SP* 626 SP (2006). ISSN: 03796566. DOI: 10.1109/EUCAP.2006.4584930.

[18] J.P. Pousi et al. "High permittivity dielectric rod waveguide as an antenna array element for millimeter waves". In: *IEEE Transactions on Antennas and Propagation* 58.3 (2010), pp. 714–719. ISSN: 0018-926X. DOI: 10.1109/TAP.2009.2039314. URL: http://ieeexplore.ieee.org/xpls/abs%7B%5C_%7Dall.jsp?arnumber=5361326.

[19] Yufeng Liu et al. "A high gain and simple-structured dielectric resonator antenna array with cylindrical rods and microstrip feeding". In: *International Journal of Applied Electromagnetics and Mechanics* 47 (2015), pp. 433–440. DOI: 10.3233/JAE-140081.

[20] Zunnurain Ahmad and Jan Hesselbarth. "Millimeterwave dielectric rod antenna with a circuit board surface mount feed". In: *GeMiC 2018 - 2018 German Microwave Conference* 2018-Janua (2018), pp. 145–147. DOI: 10.23919/GEMIC.2018.8335050.

[21] Florian Poprawa et al. "Waveguide transition to feed a fully PCB integrated dielectric rod antenna". In: *IEEE MTT-S International Microwave Symposium Digest* 2 (2010), pp. 640–643. ISSN: 0149645X. DOI: 10.1109/MWSYM.2010.5515032.

[22] Kao Cheng Huang and Zhaocheng Wang. "V-Band Patch-Fed Rod Antennas for High Data-Rate Wireless Communications". In: *IEEE Transactions on Antennas and Propagation* 54.1 (2006), pp. 297–300. ISSN: 15582221. DOI: 10.1109/TAP.2005.861521.

[23] Ta-Shing Chu and N. Kilcoyne. "The Excitation of a Dielectric-Rod Antenna by a Helix". In: *IEEE Transactions on Antennas and Propagation* 9.4 (1961), p. 2. DOI: 10.1109/TAP.1961.1145030.

[24] Anas J. Abumunshar and Kubilay Sertel. "5:1 Bandwidth Dielectric Rod Antenna Using a Novel Feed Structure". In: *IEEE Transactions on Antennas and Propagation* 65.5 (2017), pp. 2208–2214. ISSN: 0018926X. DOI: 10.1109/TAP.2017.2677379.

[25] Chia Wei Liu and Chi Chih Chen. “A UWB three-layer dielectric rod antenna with constant gain, pattern and phase center”. In: *IEEE Transactions on Antennas and Propagation* 60.10 (2012), pp. 4500–4508. ISSN: 0018926X. DOI: 10.1109/TAP.2012.2207357.

[26] Hongyu Zhou et al. “Nanoscale optical dielectric rod antenna for on-chip interconnecting networks”. In: *IEEE Transactions on Microwave Theory and Techniques* 59.10 PART 2 (2011), pp. 2624–2632. ISSN: 00189480. DOI: 10.1109/TMTT.2011.2156423.

[27] Stephen M. Hanham et al. “Evolved-profile dielectric rod antennas”. In: *IEEE Transactions on Antennas and Propagation* 59.4 (2011), pp. 1113–1122. ISSN: 0018926X. DOI: 10.1109/TAP.2011.2109689.

[28] Alejandro Rivera-lavado et al. “Increasing the bandwid dth of Dielectric Rod Waveguide An ntennas for Terahertz Applications”. In: 63.3 (2015), p. 2015.

[29] A Rivera-Lavado et al. “Dielectric Rod Waveguide Antenna as THz Emitter for Photomixing Devices”. In: *Antennas and Propagation, IEEE Transactions on* 63.3 (2015), pp. 882–890. ISSN: 0018-926X. DOI: 10.1109/TAP.2014.2387419.

[30] Federal Communications Commission. “Spectrum Frontiers R&O and FNPRM: FCC16-89”. In: (2016). ISSN: 1098-6596. DOI: 10.1017/CBO9781107415324.004. arXiv: arXiv:1011.1669v3.

[31] Dong Sik Woo, Kang Wook Kim, and Hyun-chul Choi. “A Broadband and High Gain Tapered Slot Antenna for W-Band Imaging Array Applications”. In: *International Journal of Antennas and Propagation* 2014 (2014), pp. 1–7.

[32] Y J Cheng, Y X Guo, and Z G Liu. “W-Band Large-Scale High-Gain Planar Integrated Antenna Array”. In: *Antennas and Propagation, IEEE Transactions on* 62.6 (2014), pp. 3370–3373. ISSN: 0018926X. DOI: 10.1109/TAP.2014.2310483.

[33] Nasser Ghassemi et al. “Low-cost and high-efficient W-band substrate integrated waveguide antenna array made of printed circuit board process”. In: *IEEE Transactions on Antennas and Propagation* 60.3 (2012), pp. 1648–1653. ISSN: 0018926X. DOI: 10.1109/TAP.2011.2180346.

[34] Jia Chi Samuel Chieh et al. “Millimeter-wave dual-polarized high-isolation antennas and arrays on organic substrates”. In: *IEEE Transactions on Antennas and Propagation* 61.12 (2013), pp. 5948–5957. ISSN: 0018926X. DOI: 10.1109/TAP.2013.2280872.

[35] Gildas P Gauthier et al. “A 94 GHz Aperture-Coupled Micromlachined Microstrip Antenna”. In: *MTT-S Digest* (1998), pp. 993–996.

[36] B. A. Shenouda, L. W. Pearson, and J. E. Harriss. “Etched-Silicon micromachined W-band waveguides and horn antennas”. In: *IEEE Transactions on Microwave Theory and Techniques* 49.4 I (2001), pp. 724–727. ISSN: 00189480. DOI: 10.1109/22.915450.

[37] Dong Yeon Kim et al. “High-efficiency W-band electroforming slot array antenna”. In: *IEEE Transactions on Antennas and Propagation* 63.4 (2015), pp. 1854–1857. ISSN: 0018926X. DOI: 10.1109/TAP.2015.2398129.

[38] Nasser Ghassemi and Ke Wu. “Planar high-gain dielectric-loaded antipodal linearly tapered slot antenna for E-and W-band gigabyte point-to-point wireless services”. In: *IEEE Transactions on Antennas and Propagation* 61.4 (2013), pp. 1747–1755. ISSN: 0018926X. DOI: 10.1109/TAP.2012.2232269.

[39] Yanxun Wang, Bo Bi, and Wenbin Dou. “W band axially displaced monopulse dual-reflector antenna for inter-satellite communications”. In: *IET Microwaves, Antennas & Propagation* 10.7 (2016), pp. 742–747. ISSN: 1751-8725. DOI: 10.1049/iet-map.2015.0559. URL: http://digital-library.theiet.org/content/journals/10.1049/iet-map.2015.0559.

[40] Gildas P. Gauthier, Sanjay Raman, and Gabriel M. Rebeiz. “A 90-100 GHz double-folded slot antenna”. In: *IEEE Transactions on Antennas and Propagation* 47.6 (1999), pp. 1120–1122. ISSN: 0018926X. DOI: 10.1109/8.777141.

[41] Yu Jian Cheng, Wei Hong, and Ke Wu. “94 GHz substrate integrated monopulse antenna array”. In: *IEEE Transactions on Antennas and Propagation* 60.1 (2012), pp. 121–129. ISSN: 0018926X. DOI: 10.1109/TAP.2011.2167945.

[42] C Tienda M Arrebola and J A Encinar G Toso. “Analysis of a dual-reflectarray antenna”. In: 5.September 2010 (2011), pp. 1636–1645. ISSN: 17518725. DOI: 10.1049/iet-map.2010.0444.

[43] Miao Zhang, Jiro Hirokawa, and Makoto Ando. “An E-Band Partially Corporate Feed Uniform Slot Array With Laminated Quasi Double-Layer Waveguide and Virtual PMC Terminations”. In: *IEEE Transactions on Antennas and Propagation* 59.5 (2011), pp. 1521–1527. ISSN: 0018926X. DOI: 10.1109/TAP.2011.2122301.

[44] Joon-ho So et al. “Axially symmetric dual-reflectarray antennas”. In: *Electronics Letters* 50.13 (2014), pp. 908–910. ISSN: 0013-5194. DOI: 10.1049/el.2014.0977. URL: http://digital-library.theiet.org/content/journals/10.1049/el.2014.0977.

[45] C. Migliaccio et al. “W-band high gain lens antenna for metrology and radar applications”. In: *Electron Lett* 40.22 (2004), pp. 1394–1396. DOI: 10.1049/el:20046507.

[46] Sergey Dudorov, Fritzi Topfer, and Joachim Oberhammer. “Micromachined-silicon W-band planar-lens antenna with metamaterial free-space matching”. In: *IEEE MTT-S International Microwave Symposium Digest* (2012), pp. 0–2. ISSN: 0149645X. DOI: 10.1109/MWSYM.2012.6259654.

[47] Dmitri V. Lioubtchenko et al. “Dielectric rod waveguide antenna for W band with good input match”. In: *IEEE Microwave and Wireless Components Letters* 15.1 (2005), pp. 4–6. ISSN: 15311309. DOI: 10.1109/LMWC.2004.840946.

[48] A A Generalov, D V Liou, and A V Räisänen. “Dielectric Rod Waveguide Antenna at 75 – 1100 GHz”. In: *7th European Conference on Antennas and Propagation (EUCAP 2013)* Eucap (2013), pp. 541–544.

[49] Andrey A. Generalov et al. “Wide Band mm- and Sub-mm-Wave Dielectric Rod Waveguide Antenna”. In: *IEEE Transactions on Terahertz Science and Technology* 4.5 (2014), pp. 1–7. ISSN: 2156-342X. DOI: 10.1109/TTHZ.2014.2342503. URL: http://ieeexplore.ieee.org/lpdocs/epic03/wrapper.htm?arnumber=6876054.

[50] N Trinh Trang, Raj Mittra, and J Roy Paleta. “Horn Image Guide Leaky-wave Antenna”. In: *IEEE Transactions on Microwave Theory and Techniques* (1981), pp. 1310–1314.

[51] D. G. Kiely. *Dielectric Aerials*. Methuen and Company, 1953.

[52] D. Hondros and P. Debye. “Elektromagnetische Wellen an dielektrischen Drähten”. In: *Annalen der Physik* 337.8 (1910), pp. 465–476. ISSN: 15213889. DOI: 10.1002/andp.19103370802.

[53] D.F. Halliday and D. G. Kiely. “Dielectric Rod Aerials”. In: *Journal of the Institution of Electrical Engineers - Part IIIA: Radiocommunication* 94 (1947), pp. 610–618.

[54] Gilbert Wilkes. “Wavelength Lenses”. In: *Proceedings of the IRE* 36.2 (1948), pp. 206–212. ISSN: 00968390. DOI: 10.1109/JRPROC.1948.233272.

[55] R. B. Watson and C. W. Horton. “The radiation patterns of dielectric rods - Experiment and theory”. In: *Journal of Applied Physics* 19.7 (1948), pp. 661–670. ISSN: 00218979. DOI: 10.1063/1.1698188.

[56] Maurice Bouix. “Contribution a l’étude des antennes diélectriques”. In: *Annales des Telecommunications* 7.6 (1952), pp. 276–295. ISSN: 1958-9395. DOI: 10.1007/BF03014498.

[57] A.Z. FRADIN. “Dielectric Antennas”. In: *Microwave Antennas* (1961), pp. 511–584. DOI: 10.1016/b978-0-08-009434-2.50013-8.

[58] J Brown and J O Spector. “The radiating properties of end-fire aerials”. In: *Proc. IEE* 2216 (1957), pp. 27–34.

[59] J.R. James. “Theoretical investigation of cylindrical dielectric-rod antennas”. In: *Proceedings of the Institution of Electrical Engineers* 114.3 (1967), pp. 309–319. ISSN: 00203270. DOI: 10.1049/piee.1967.0317.

[60] Takashi Ando, Junji Yamauchi, and Hisamatsu Nakano. “Numerical analysis of a dielectric rod antenna - Demonstration of the discontinuity-radiation concept”. In: *IEEE Transactions on Antennas and Propagation* 51.8 (2003), pp. 2007–2013. ISSN: 0018926X. DOI: 10.1109/TAP.2003.814731.

[61] R. B. Watson and C. W. Horton. “On the calculation of radiation patterns of dielectric rods”. In: *Journal of Applied Physics* 19.9 (1948), pp. 836–837. ISSN: 00218979. DOI: 10.1063/1.1698215.

[62] C. W. Horton, F. C. Karal, and C. M. McKinney. “On the radiation patterns of dielectric rods of circular cross section - The TM01 mode”. In: *Journal of Applied Physics* 21.12 (1950), pp. 1279–1283. ISSN: 00218979. DOI: 10.1063/1.1699590.

[63] C. H. Chandler. “An investigation of dielectric rod as wave guide”. In: *Journal of Applied Physics* 20.12 (1949), pp. 1188–1192. ISSN: 00218979. DOI: 10.1063/1.1698306.

[64] Walter M. Elsasser. “Attenuation in a dielectric circular rod”. In: *Journal of Applied Physics* 20.12 (1949), pp. 1193–1196. ISSN: 00218979. DOI: 10.1063/1.1698307.

[65] B. Thomas. “The Precise Mechanism of Radiation from Surface Wave Aerials”. In: *The Journal of the Institution of Engineers, Australia* 9.36 (1964), pp. 225–238.

[66] J.C. Simon and G. Weill. “Un Nouveau Type D’Aerien A Rayonnement Longitudinal”. In: *Annales De Radioelectricite* July.33 (1953), pp. 183–198.

[67] Morton Michael Astrahan. “Guided Waves on Hollow Dielectric Tubes”. Dissertation. Northwestern University, 1949.

[68] William Chester Jr. Jakes. “Attenuation and Radiation Characteristics of Dielectric Tube Waveguides”. Dissertation. Northwestern University, 1949.

[69] Kao Cheng Huang and Zhaocheng Wang. “Millimeter-Wave Circular Polarized Beam- Steering Antenna Array for Gigabit Wireless Communications”. In: *IEEE Transactions on Antennas and Propagation* 54.2 (2006), pp. 743–746. ISSN: 15582221. DOI: 10.1109/TAP.2005.863158.

[70] Y Liu, X Chen, and Acad Electromagnet. “A Novel Microstrip-fed Dielectric ROD Antenna Array with High Gain”. In: *Piers 2012 Moscow: Progress in Electromagnetics Research Symposium* 1 (2012), pp. 1187–1190. ISSN: 15599450. URL: %7B%5C%%7D3CGo%7B%5C%%7D0Ato.

[71] Constantine A. Balanis. *Advanced Engineering Electromagnetics*. Second Edi. John Wiley & Sons, Inc., 2012, p. 1040. ISBN: 978-0-470-58948-9.

[72] H. Ehrenspeck and H. Poehler. “A new method for obtaining maximum gain from yagi antennas”. In: *IRE Transactions on Antennas and Propagation* 7.4 (Oct. 1959), pp. 379–386. ISSN: 0096-1973. DOI: 10.1109/TAP.1959.1144708. URL: http://ieeexplore.ieee.org/document/1144708/.

[73] Rainee N. Simons. *Conventional Coplanar Waveguide*. Vol. 7. 2003, pp. 11–86. ISBN: 0471161217. DOI: 10.1002/0471224758.ch2.

[74] Sergey Dudorov. “Rectangular dielectric waveguide and its optimal transition to a metal waveguide”. In: *PhD Thesis, Helsinki University of Technology, Helsinki* (2002), p. 91.

[75] J.R. James. “Engineering approach to the design of tapered dielectric-rod and horn antennas”. In: *Radio and Electronic Engineer* 42.6 (1972), p. 251. ISSN: 00337722. DOI: 10.1049/ree.1972.0042. URL: http://digital-library.theiet.org/content/journals/10.1049/ree.1972.0042.

[76] Kao-cheng Huang and John Thornton. “Polyrod antennas”. In: *Modern Lens Antennas for Communications Engineering*. 1st ed. 2012, pp. 77–112. ISBN: 9781118345146.

[77] T. Ando et al. “Linearly and curvilinearly tapered cylindrical- dielectric-rod antennas”. In: *IEEE Transactions on Antennas and Propagation* 53.9 (2005), pp. 2827–2833. ISSN: 0018-926X. DOI: 10.1109/TAP.2005.854551.

[78] Francis J. Zucker and John A. Strom. “Experimental Resolution of Surface-Wave Antenna Radiation into Feed and Terminal Patterns”. In: *IEEE Transactions on Antennas and Propagation* AP-18.3 (1970), pp. 420–422. ISSN: 15582221. DOI: 10.1109/TAP.1970.1139689. URL: http://mhebooklibrary.com/doi/book/10.1036/0071475745.

[79] Denise C. Lugo et al. “Low permittivity cladding to improve the performance of dielectric rod waveguides and dielectric end-fire antennas”. In: *IEEE MTT-S International Microwave Symposium Digest* 2016-Augus (2016), pp. 16–18. ISSN: 0149645X. DOI: 10.1109/MWSYM.2016.7540010.

Appendix A: Copyright Permissions

This is the IEEE guidance on use of previously published material for use in a dissertation. This is related to Chapter 6.

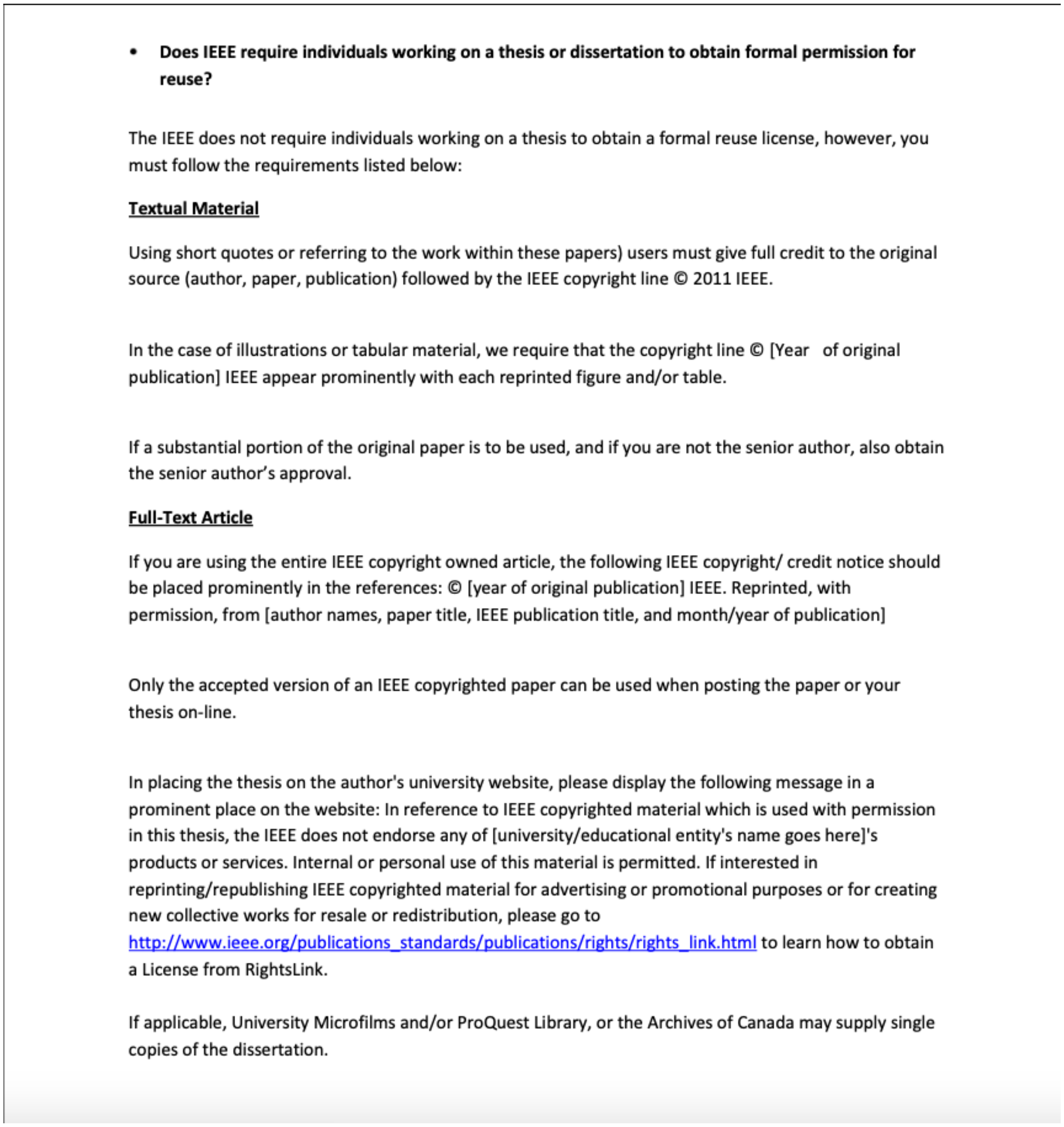

- **Does IEEE require individuals working on a thesis or dissertation to obtain formal permission for reuse?**

The IEEE does not require individuals working on a thesis to obtain a formal reuse license, however, you must follow the requirements listed below:

Textual Material

Using short quotes or referring to the work within these papers) users must give full credit to the original source (author, paper, publication) followed by the IEEE copyright line © 2011 IEEE.

In the case of illustrations or tabular material, we require that the copyright line © [Year of original publication] IEEE appear prominently with each reprinted figure and/or table.

If a substantial portion of the original paper is to be used, and if you are not the senior author, also obtain the senior author's approval.

Full-Text Article

If you are using the entire IEEE copyright owned article, the following IEEE copyright/ credit notice should be placed prominently in the references: © [year of original publication] IEEE. Reprinted, with permission, from [author names, paper title, IEEE publication title, and month/year of publication]

Only the accepted version of an IEEE copyrighted paper can be used when posting the paper or your thesis on-line.

In placing the thesis on the author's university website, please display the following message in a prominent place on the website: In reference to IEEE copyrighted material which is used with permission in this thesis, the IEEE does not endorse any of [university/educational entity's name goes here]'s products or services. Internal or personal use of this material is permitted. If interested in reprinting/republishing IEEE copyrighted material for advertising or promotional purposes or for creating new collective works for resale or redistribution, please go to http://www.ieee.org/publications_standards/publications/rights/rights_link.html to learn how to obtain a License from RightsLink.

If applicable, University Microfilms and/or ProQuest Library, or the Archives of Canada may supply single copies of the dissertation.

Appendix B: Design Code (Python)

```
###################################################
# Solution for Dielectric Rod Attenuation
# Individual Solutions
# 16 Nov 18
# Gabriel Saffold
# Python
###################################################

# Import

from scipy import optimize
from scipy import special
import matplotlib.pyplot as plt
import numpy as np

# Constants
f = 15e9 # 15GHz for Ku band
c = .3e9
lam_0 = c/f
#n = 0 # for Transverse Electric and Magnetic Modes
n = 1 # for the Dipole Mode
eps1 = 10.2      # Rogers 3010 Rod Material: er = 10.2
eps2 = [1,1.6,2.6] # ABS Cladding dielectric constant (1 (air), 1.6 (50% infil
    ABS), 2.6 (100% infil ABS))
q = np.arange(0.01,10,0.0005)
target = [1.00, 1.03, 1.3] # Target lamda/lambda_z values for end of Terminal
   Taper, Constant Cross-section, and Feed diameters, respectively [1.00,
   1.02, 1.3]

# Definitions
omega = 2*np.pi*f
eps = np.divide(eps1,eps2)
d_lam_x = np.empty(q.size)
lam = np.empty(len(eps2))
U_y = np.empty(q.size)
A = np.empty((len(eps2),len(target)))
U1 = np.empty((len(eps2),len(target)))
D = np.empty((len(eps2),len(target)))
y = np.empty((len(eps2),len(target)))
FT = 2
CC = 1
TT = 0

# Calculations
for j in range(0,len(eps2)):
```

```
z = 0
lam = lam_0/np.sqrt(eps2[j])
for i in range(0,len(q)):
    # Dipole Mode: n=1
    def solver(x):
        p = x
        f = special.jvp(1,p,1)/(p*special.jv(1,p))
        g = special.kvp(1,q[i],1)/(q[i]*special.kv(1,q[i]))
        return (((eps[j]*f)+g)*(f+g)-((n**2)*(eps[j]/p**2+1/q[
            i]**2)*(1/p**2+1/q[i]**2)))
    p = optimize.root(solver,1)
    d_lam = np.sqrt((p.x**2+q[i]**2)/(eps[j]-1))*(1/np.pi)
    U = np.sqrt(((eps[j]/p.x**2)+(1/q[i]**2))/((1/p.x**2)+(1/q[i
        ]**2)))
    U_y[i] = U
    d_lam_x[i] = d_lam

    for k in range(z,len(target)):
        if 0.999<U_y[i]/target[k]<1.001:
            A[j,k] = (d_lam_x[i]*lam/1.13)**2
            U1[j,k] = U_y[i]
            D[j,k] = d_lam_x[i]
            print('\n',A[j,k], '      ', U1[j,k],'      ', D[j
                ,k])
            z = z + 1

x = np.sqrt(A[j,FT]/2)
print('\n', 'epsilon_clad = ', eps2[j], ':\n')
length = 6*lam
FeedTaper = lam*1.6
TermTaper = lam*0.5
print('Antenna Length = ', length*1000, ' mm')
print('Feed Taper Length = ', FeedTaper*1000, ' mm')
print('Terminal Taper Length = ', TermTaper*1000, ' mm')
print('Effective Wavelength = ', lam*1000, ' mm')
# Feed Taper
y[j,0] = 2*x
print('Feed Taper:\n','lam/lam_z = ',U1[j,FT],'\n','d/lam = ',D[j,FT],
     '\n', 'Area = ', A[j,FT], '\n', 'Thickness = ', x*1000,' mm\n','
    Height =', y[j,0]*1000,' mm\n')
# Constant Cross Section
y[j,1] = A[j,CC]/x
# Terminal Taper
print('Const Cross Sec:\n','lam/lam_z = ',U1[j,CC],'\n','d/lam = ',D[j
    ,CC], '\n', 'Area = ', A[j,CC],'\n', 'Thickness = ', x*1000,' mm\n
    ', 'Height = ', y[j,1]*1000, ' mm\n')
y[j,2] = A[j,TT]/x
print('Term Taper:\n','lam/lam_z = ',U1[j,TT],'\n','d/lam = ',D[j,TT],
     '\n', 'Area = ', A[j,TT],'\n', 'Thickness = ', x*1000,' mm\n', '
    Height = ', y[j,2]*1000, ' mm\n')

plt.plot(d_lam_x,U_y, label = '$Cladding: \epsilon_{clad} = $%.1f' %
    eps2[j])
```

```
#Plot
plt.axis([0,1,1,3])
plt.legend(loc=4, prop={'size': 16})
plt.ylabel('$\lambda_{clad} / \lambda_{rod}$', fontsize='18')
plt.xlabel('$d / \lambda_{clad}$', fontsize='18')
plt.tick_params(axis = 'both', which = 'major', labelsize = 18)
plt.show()
```